A Multi-omic Atlas of Human Choroid Plexus in Alzheimer's Disease

Tristan J. Philippe[1], Denis R. Avey [1,2], Nicola A. Kearns [1,2], Himanshu Vyas[1], Sashini De Tissera[1], Jishu Xu[1], Bernard Ng[1], Devin M. Saunders[1], Amiko K. Lagrimas[1], Duc Duong[3], Nicholas T. Seyfried[3], David A. Bennett[1,2], Yanling Wang[1,2]

1. Rush Alzheimer's Disease Center, Rush University Medical Center, Chicago, IL, 60612, USA
2. Department of Neurological Sciences, Rush University Medical Center, Chicago, IL, 60612, USA
3. Emory University School of Medicine, Atlanta, GA 30322, USA

*Correspondence to Yanling_Wang@rush.edu

Abstract

The choroid plexus (CP) regulates barrier integrity, cerebrospinal-fluid (CSF) dynamics, and immune surveillance, yet its role in Alzheimer's disease (AD) remains poorly defined. We performed snRNA-seq on CP samples from 69 ROSMAP participants spanning normal cognition, mild cognitive impairment, and AD dementia, and integrated these data with spatial transcriptomics, snATAC-seq, and proteomics from CP tissue and CSF. We identified 17 CP cell states and uncovered widespread disease-associated transitions that converged into three major phenotypic axes. Along the inflammatory axis, epithelial cells and border-associated macrophages (BAMs) showed progressive immune activation, with BAMs shifting from inflammatory to stress-dominant states. In the barrier axis, epithelial cells, fibroblasts, and endothelial cells exhibited reduced junction-related gene expression and broad alterations in transport pathways. Epithelial cells also showed late-stage cilia loss and CSF-regulatory pathway impairment, indicating a breakdown in epithelial polarity and CSF sensing, consistent with abnormal CSF proteomic signatures. Along the remodeling axis, fibroblasts showed bidirectional ECM alterations, while epithelial and stromal cells demonstrated aberrant cell–matrix adhesion pathways. Spatial neighborhood analysis revealed a multicellular signaling hub, with epithelial-rich niches showing the strongest dysregulation in AD. Together, these findings define a unified model of CP dysfunction in AD and position the CP as an active, multicellular contributor to AD pathophysiology.

Introduction

The choroid plexus (CP) has traditionally been viewed as a supporting structure that forms the interface between the brain and periphery, producing cerebrospinal fluid (CSF). However, emerging evidence suggests that the CP is a dynamic regulator of brain homeostasis, modulating barrier permeability, molecular transport, metabolism, and immune surveillance[1–4]. Disruption of CP function has been implicated in impaired CSF flow, barrier breakdown, and neuroinflammation—processes that are highly relevant to Alzheimer's disease (AD)[5–7].

Despite these links, the CP has received considerably less attention in AD research than the brain parenchyma. Studies using animal models or human tissue suggest that CP barrier integrity and function are altered in AD, potentially affecting immune cell trafficking and the clearance of pathological proteins[8–15]. However, a comprehensive understanding of how human CP cell states shift along the clinical continuum from no cognitive impairment (NCI) to mild cognitive impairment (MCI) and Alzheimer's dementia (ADd) remains lacking.

To address this gap, we applied high-resolution single-cell multi-omics and spatial transcriptomics to construct a detailed atlas of CP alterations across NCI, MCI, and ADd individuals from the Religious Orders Study or Rush Memory and Aging Project (ROSMAP)[16]. Our analysis reveals coordinated cell state differences in epithelial, immune, endothelial, and fibroblast populations that collectively reshape the CP's immune, barrier, and stromal landscape during disease progression, offering new mechanistic insights into how CP dysfunction contributes to AD pathophysiology.

Results

Major cell classes of the human choroid plexus

To transcriptionally characterize the CP cell types and states, we performed snRNA-seq on 69 individuals (NCI=21, MCI=21, and ADd=27; Fig. 1a-b; Extended Data table 1). After quality control and doublet removal, we recovered 758,302 total nuclei. Based on canonical markers, we annotated cell clusters and detected five major CP cell types, including epithelial (*TTR*, *HTR2C*), fibroblast (*DCN*, *LEPR*, *FN1*), endothelial (*PECAM1*, *VWF*, *INSR*), mural (*ACTA2*, *TAGLN*, *MYH11*), and immune (*CD163*, *STAB1*, *MSR1*) populations (Fig. 1c–d, Extended Data table 2). Gene detection per nucleus was consistent with previous postmortem human snRNA-seq studies[18–20] (Extended Data Fig. 1a-c), and no significant cell-type proportion differences were observed between NCI, MCI and ADd groups (Fig. 1e Extended Data table 3).

82 We next validated the major CP cell types by multiplex immunohistochemistry. Consistent with previous
83 human histological studies[21], we detected TTR$^+$ epithelial cells forming the luminal boundary, DCN$^+$ fibroblasts
84 enriched in stromal regions, CD31/PECAM1$^+$ endothelial cells comprising small and large vessels, SMA$^+$ mural
85 cells constituting the large vessel wall, and CD45$^+$ immune cells dispersed across stromal and epithelial
86 compartments (Fig. 1f). Together, these results confirm the identity of major CP cell types and highlight the
87 widespread presence of immune cells across stromal and vascular compartments.
88
89 To validate marker gene expression and spatially contextualize these findings, we applied spatial gene profiling
90 using the CosMx Spatial Molecular Imager on CP sections from eight individuals (NCI=4; AD=4; Extended
91 Data table 1, Fig 1i, upper left) with the 6K human discovery panel. After excluding low-quality or mis-
92 segmented cells, we obtained 106,556 high-quality cells for analysis. Unbiased clustering and annotation
93 revealed the same major CP cell types identified in snRNA-seq (Fig. 1g, Extended Data Fig 1d-i, Extended Data
94 table 4), with no significant differences in cell-type proportions between NCI and AD (Fig. 1h, Extended Data
95 table 5). We confirmed the expected localization of annotated cell types, including epithelial, fibroblast,
96 endothelial, mural, and immune cells (Fig. 1i, top). At the gene level, canonical markers were enriched in their
97 expected cell types: *TTR*, *HTR2C*, and *GPX3* in epithelial cells; *DCN*, *FN1*, and *LEPR* in fibroblasts; *VWF*,
98 *PECAM1*, and *INSR* in endothelial cells; *MYH11*, *TAGLN*, and *ACTA2* in mural cells; and *STAB1*, *CD163*, and
99 *MSR1* in immune cells (Fig. 1i, bottom). These data validate cell-type assignments and demonstrate the spatial
100 organization of CP cellular compartments.
101
102 We conducted multi-omic profiling (snATAC-seq with matched snRNA-seq) in a subset of cases (n=6) to
103 assess chromatin accessibility alongside gene expression. After standard QC, UMAP clustering identified major
104 epithelial, fibroblast and immune clusters, with ATAC accessibility patterns concordant with RNA-based cell
105 type assignments (Extended Data Fig. k-q, Extended Data table 6).
106
107 **Epithelial cells exhibit progressive inflammatory activation and late ciliary dysfunction in the choroid**
108 **plexus across disease stages**
109 We subclustered CP epithelial cells into four transcriptionally distinct epithelial subtypes: Epi_1a, Epi_1b,
110 Epi_2a, and Epi_2b (Fig. 2a-e, Extended Data Fig. 2a-d, and tables 7-9). Epi_2a/2b were enriched for transport
111 and secretory genes (*TTR*, *AQP1*, *SLC25A6*, *SLC25A23*, *SLC4A2*), and Epi_1a/1b were enriched for
112 cytoskeletal *(KRT8*, *KRT18),* adhesion (*CDH1)*, and ciliogenesis signatures (*DNAH6*, *CFAP100*, *CFAP69*).
113 Within the secretory population, Epi_2a also showed strong ciliogenesis signatures, while Epi_2b expressed
114 fewer cilia genes, consistent with a shift from ciliated to less-ciliated secretory states (Fig. 2b). Epi_2a/2b
115 showed higher tight-junction proteins (*CLDN1/5*, *OCLN*) and greater mitochondrial gene expression (*MT-CO1*,
116 *MT-CO2*, *MT-CO3*), in line with enhanced metabolic need for secretory states (Fig. 2b, Extended Data table 7).

117 Functional annotation further aligned with marker gene profiles: Epi_1a/1b were enriched for microtubule
118 projection and cytoskeletal organization; Epi_1b/2a were associated with cilium assembly; and Epi_2b was
119 enriched for transport and metabolic processes (Fig. 2c).
120
121 Unsupervised clustering across spatial transcriptomics (ST) and ATAC-seq consistently identified four major
122 epithelial subclusters (Fig. 2d, Extended data Table 8; Extended Data Fig. 2a-d and Table 8-9). Although
123 individual marker genes showed variable assignments across data types, likely reflecting modality-specific
124 resolution, the core functional identities of the clusters were preserved, with KRT-high epithelial cells
125 corresponding to Epi_1a and ciliated to less-ciliated secretory states within Epi_1a/2a/2b (Fig. 2d–e, Extended
126 Data Table 8-9; Extended Data Fig. 2a-d).
127
128 Importantly, the relative proportions of the four epithelial subclusters were stable across NCI, MCI, and ADd in
129 our snRNA-seq and ST data (Fig. 2f-g, Extended Data Table 3 and 5), indicating that epithelial heterogeneity
130 itself is not disease-associated. We next examined transcriptome differences across AD disease progression at
131 both the aggregated epithelial cell level and within individual epithelial subtypes. Along the disease trajectory
132 from NCI to MCI to ADd, we detected progressive upregulation of immune and inflammatory genes (e.g. *IL6R*
133 and *SERPINE3*). However, we observed a marked downregulation of cilia-related genes (e.g. *CROCC*, *FOXJ1*,
134 *TUBA1A*, and *CFAP43*) that correlated with cognitive decline (Extended Data Fig. 2e and Table 10-11). Gene
135 set enrichment analysis revealed that immune responses, secretion, and transporter activities were progressively
136 higher from NCI to ADd, whereas cilia-related pathways were selectively lower in ADd (Fig. 2h). At the
137 epithelial subtype level, Epi_1a/2a carried the strongest signatures of both immune activation and cilia loss (Fig.
138 2h). ST corroborated these findings at the aggregated epithelial cell level (Fig 2h right and Extended Data Table
139 12).
140
141 To resolve disease temporal patterns, we used template matching[22] to classify disease-associated transcriptional
142 programs into different patterns and identified two major categories: progressive differences included immune
143 and transporter genes (e.g., *SLC17A5*, *IL6R*; Fig. 2i), while late-stage changes were dominated by cilia-related
144 genes (*CROCC*, *FOXJ1*, *TUBA4A*; Fig. 2i and Extended Data Table 10). ST corroborated these findings,
145 revealing reduced cilia gene expression (*FOXJ1*, *TUBA4A*) in ADd epithelium (Fig. 2j). Chromatin accessibility
146 profiling by snATAC-seq further validated these observations, showing less accessibility at key cilia-related
147 transcription factor loci (e.g. *FOXJ1, KLF4)*) and correspondingly structural gene loci (*CROCC,*
148 *DYNC1H1* and *TUBA4A*), consistent with their transcriptional downregulation (Fig. 2k, Extended Data Table
149 13). Immunohistochemistry confirmed a reduction of ciliary rootlets, with CROCC staining markedly lower in
150 AD relative to controls (Fig. 2l).
151

152 Since the CP epithelium is a key tissue interface with CSF, we next examined protein expression in CSF using
153 the Olink Explore platform (n=27), which enabled measurement of 2,884 proteins (Fig. 2m, upper). This
154 analysis revealed stage-dependent differences that paralleled the transcriptomic findings. At the early stage of
155 AD progression, we observed more inflammatory signatures, including enrichment of monocyte chemotaxis and
156 chemokine activity pathways (Fig. 2m). By the late stage, we detected lower cilium-related terms and multiple
157 metabolic processes, including proteasomal and collagen catabolism (Fig. 2m; Extended Data Table 14).
158 Together, these data highlight coordinated molecular changes between CP epithelial cells and the CSF
159 proteome, reinforcing the role of the CP as a dynamic interface linking inflammation and impaired CSF
160 secretion mechanisms in AD.
161

162 **Border-associated macrophages shifted from inflammatory to stress-associated states in the choroid**
163 **plexus across disease stages**

164 We next examined immune cells in the CP. Multiplex fluorescent imaging confirmed the presence of $CD163^+$
165 macrophages and $CD3^+$ T cells within the ECAD+ CP tissue (Fig. 3a). Subclustering of snRNA-seq data
166 identified three states of border-associated macrophages (BAM_1-3) and a small T-cell population marked by
167 expression of *THEMIS* and *CD3E* (Fig. 3b). BAM_1 expressed *CD163*, *MRC1*, *LYVE1*, and *IL4R*, consistent
168 with an immune-activated state. BAM_2 was enriched for heat-shock protein genes (*HSPA1A*, *HSP90AA1*,
169 *DNAJA1*), indicative of a stress-adapted phenotype, while BAM_3 expressed *MKI67* and *CENPF*, reflecting a
170 proliferative subset. Functional enrichment supported these distinctions: BAM_1 was associated with immune
171 activation and cytokine release, BAM_2 with protein folding and stress responses, and BAM_3 with cell cycle
172 and proliferation (Fig. 3c-d, Extended Data Table 15). snATAC-seq revealed selective chromatin accessibility
173 at *DNAJA1* and *HSPA8* loci within the BAM2 subcluster, consistent with their elevated transcription (Fig. 3e,
174 Extended Data Fig. 3a-b and Table 16). Notably, BAM1- and BAM2-specific transcriptional signatures
175 corresponded with distinct ATAC activity, indicating coordinated regulation of chromatin accessibility and
176 gene expression across BAM states (Fig. 3f). Because of limited immune cell numbers, we applied a supervised
177 approach[23] to annotate ST subclusters, which showed strong correspondence with snRNA-seq–defined BAM
178 populations (Fig. 3g-h, Extended data Fig 3c). When mapped back to the CP, BAM1, BAM2, BAM3, and T
179 cells were broadly distributed, confirming the presence of these immune populations throughout the tissue (Fig.
180 3h).
181

182 Notably, we observed higher BAM_2 proportions in ADd (Fig. 3i, Extended Data Table 3), indicating a shifted
183 state toward a stress-dominant phenotype. At the pathway level, we observed progressively stronger immune
184 responses across disease stages, including enrichment of pathways such as antigen presentation, leukocyte
185 proliferation, and other signatures of immune activation. In ADd, we also detected enrichment of unfolded
186 protein binding, indicative of stress responses, consistent with the expansion of the BAM_2 population

187 characterized by high expression of heat shock proteins (Fig. 3j). At the gene level, we observed stage-
188 dependent regulation of classical immune-related genes, including *HLA-DRA*, as well as additional immune-
189 associated genes linked to CP function, such as *CDC42SE1*, *LY75*, *TRIM14*, and *MR1* in early stages,
190 and *LPAR1*, *TNFAIP2*, *CDC42*, and *HSPA1*A in late stages (Fig. 3k, Extended Data Table 17). Spatial
191 transcriptomics data confirmed increased *HSP* expression, along with elevated *CD68* and *HLA-*
192 *DRA/DRB* expression in AD (Fig. 3j, right and l-m, Extended Data Table 18). Immunostaining further validated
193 these findings, showing higher HLA-DR and CD68 intensity in $CD163^+$ macrophages in AD compared with
194 NCI (Fig. 3n). However, we did not observe significant differences in the number of total T cells, $CD4^+$ T cells,
195 or $CD8^+$ cells in AD (Fig. 3o, Extended Data Fig. 3d). Together, these results demonstrate that immune cells in
196 the CP are heterogeneous and undergo progressive immune activation and stress responses across disease
197 stages.
198
199 **Fibroblast remodeling in the choroid plexus in AD dementia**
200 To characterize fibroblast heterogeneity in the CP, we subclustered fibroblasts into three transcriptional
201 subtypes (Fib_1, Fib_2, Fib_3; Fig. 4a). Fib_1 expressed markers such as *LEPR*, *PLXNA4*, and *STXBP6*,
202 consistent with regulatory and signaling functions. Fib_2 was enriched for *CLDN11*, *TJP1, ITGBL1, GJB6,*
203 *TRPM3*, and *ROBO1*, indictive of tight-junction-expressing barrier-like fibroblasts. Fib_3 expressed *DCN*, *FN1*,
204 *FBLN1*, *CDH11*, and multiple collagens (e.g., *COL4A2*, *COL3A1*, *COL6A3*), indicative of extracellular-matrix
205 (ECM)-producing fibroblasts (Fig. 4b, Extended Data Table 19). Recent work identified a population of "base
206 barrier" fibroblasts in the mouse CP using scRNA-seq[2], describing them as a barrier-forming population at the
207 stroma–CSF interface. While similar gene signatures were noted in a published human dataset[19], those base
208 barrier fibroblasts had not been independently resolved in human tissue due to limited sampling. Our study
209 extends these findings using unbiased clustering of a larger cohort, resolving Fibro_2 as the human counterpart
210 of this base barrier fibroblast population. Immunohistochemistry staining confirmed that $CLDN11^+$
211 Fibro_2 localized to the basal side of the CP epithelium, particularly around larger vessels (CD31, SMA)
212 adjacent to the brain parenchyma, consistent with a barrier-supporting niche (Fig. 4c).
213
214 Despite these molecular distinctions, gene ontology enrichment showed broad overlap across fibroblast
215 subtypes, with shared programs in adhesion, ECM organization, and ion transport (Extended Data Fig. 4a).We
216 then applied the same supervised approach[23] to annotate ST fibroblast subclusters, which showed strong
217 correspondence with snRNA-seq–defined populations (Extended Data Fig. 4b; Fig. 4d) and mapped to original
218 locations within the CP (Fig. 4e).
219
220 We next examined disease-associated transcriptional differences at the fibroblast subtype level. Fibroblast
221 proportions were similar across NCI, MCI, and ADd (Fig. 4f), indicating that disease progression does not alter

222 relative abundance but instead drives transcriptional reprogramming within each subtype. Gene set enrichment
223 analyses in fibroblasts revealed apparently bidirectional differences across major pathways in both early and
224 late disease stages, reflecting heterogeneous transcriptional remodeling (Fig. 4g and Extended Data Table 20-
225 21). Tight junction and cell adhesion pathways showed overall negative enrichment, indicating weakened
226 barrier integrity. By contrast, cell–matrix adhesion, transporter, and ion channel pathways displayed positive
227 enrichment at late stage, indicating an adaptive transcriptional response. Among fibroblast subtypes,
228 Fibro_2 showed the most consistent upregulation of ECM- and transporter-related pathways whereas
229 Fibro_1 and Fibro_3 exhibited more transcriptional downregulation. At the tissue level, ST data revealed a
230 general downregulation of transporter and ion channel activity and upregulation of ECM remodeling. Together,
231 these findings indicate that fibroblast remodeling in ADd involves broad, bidirectional transcriptional changes,
232 with consistent tight junction loss and selective ECM remodeling.
233
234 To further resolve temporal differences, we examined gene expression patterns in fibroblasts. Several collagen-
235 related genes, including *ADAMTS9*, *COL15A1*, and *LAMA2*, were progressively upregulated, consistent with
236 greater ECM deposition, whereas others, such as *COL8A1*, were downregulated, indicating selective collagen
237 loss (Fig. 4h Extended Data Fig. 4c). Similarly, transporter genes, such as SLC family (*SLC25A8*, *SLC16A4*,
238 *SLC16A9*), also exhibited bidirectional regulation, highlighting heterogeneous shifts in ion and metabolite
239 handling. To examine stage-dependent transcriptional dynamics, we compared differentially expressed genes
240 (DEGs) across fibroblast subtypes at each disease stage. The overlap between DEGs across stages was mild to
241 moderate, suggesting progressive but partly distinct transcriptional alterations during disease progression.
242 Similarly, when comparing ADd versus NCI across different fibroblast subtypes, only limited overlap was
243 observed, indicating that each fibroblast subtype exhibits partially unique transcriptional responses to AD
244 pathology (Extended Data Fig. 4d-e).
245
246 ST analysis confirmed these fibroblast-specific transcriptional changes in AD, with increased *ADAMTS9*,
247 *COL15A1*, and *LAMA2* expression and reduced *COL8A1* relative to controls (Fig. 4i). To validate these findings
248 at the histological level, we performed Movat's pentachrome staining, followed by color deconvolution and
249 ECM threshold masking to quantify collagen deposition (Fig. 4j). The density distribution analysis revealed a
250 subtle shift from low- to high-collagen regions in AD and MCI compared with NCI although this trend did not
251 reach statistical significance (Fig. 4j).
252
253 **Endothelial and mural cell dysregulation in the choroid plexus in AD dementia**
254 We next investigated vascular compartments of the CP, focusing on endothelial and mural cells. We identified
255 three endothelial subtypes (Endo_1, Endo_2, Endo_3) and three mural subtypes (Mural_1, Mural_2, Mural_3.
256 Endo_1 was characterized by strong *PECAM1*, *CLDN5*, and *CDH13* expression with lower *VWF*, consistent

with an arterial/arteriolar endothelial identity. Endo_2 also expressed *CLDN5* but showed higher *VWF* together with *CEMIP2*, *IL1R1*, and *IL4R*, consistent with a venous endothelial phenotype. Endo_3 was distinguished by robust *PLVAP* and *FLT1* expression, consistent with fenestrated capillary endothelium in the CP (Fig 5a-b, Extended Data Table 22). Mural_1 expressed high levels of canonical contractile smooth muscle markers, including *ACTA2*, *MYH11*, *TPM1*, and *MYOCD*, consistent with arterial smooth muscle cells. Mural_2 showed lower expression of contractile genes but enrichment of ECM-remodeling transcripts such as *COL18A1*, *ADAMTS9*, and *CRISPLD2*, indicative of a venous smooth muscle or transitional phenotype. Mural_3 exhibited reduced expression of smooth muscle genes and upregulation of signaling and matrix regulators such as *CEMIP*, *PLXDC2*, and *ENPP2*, consistent with a pericyte identity associated with capillaries (Fig 5c-d, Extended Data Table 23). We then applied the same supervised approach[23] to identify ST vascular subtypes, which showed strong correspondence with snRNA-seq–defined populations (Fig. 5e) and mapped to vascular niches within the CP (Fig. 5g).

We next asked how mural subtypes are positioned relative to endothelial populations (Fig. 4f). Mural_1, which we annotated as arterial smooth muscle cells, was preferentially associated with Endo_1 (arterial endothelium). By contrast, Mural_3, defined as pericytes, showed enrichment near Endo_3, corresponding to fenestrated capillary endothelium. These relationships indicate coordinated arterial and capillary compartmentalization between endothelial and mural cells in the choroid plexus.

To validate the endothelial subtype classification, we performed immunostaining with CLDN5 and PLVAP together with SMA and CAV to visualize vascular structure (Fig. 4h). CLDN5 was strongly expressed in arteries and veins, whereas PLVAP was selectively enriched in capillaries. Arteries and veins were further distinguished by mural SMA staining, with arteries showing thick, robust expression and veins exhibiting thinner signals. These findings confirmed that CLDN5 and PLVAP are reliable markers for distinguishing arterial/venous from capillary endothelial cells. The endothelial cell representation did not differ across NCI, MCI, and ADd groups, whereas mural populations had a lower Mural_3 subtype in ADd (Fig. 5f). Given the pericyte-like transcriptional profile of Mural_3, this decrease may reflect pericyte loss or dedifferentiation, indicating vascular instability and barrier dysfunction in ADd. Correspondingly, differential expression analyses in snRNA-seq and ST revealed progressive reductions in junctional and actin-binding pathways, along with downregulation of ion transport signatures, consistent with progressive barrier weakening in ADd (Extended Data Tables 24-27).

Transcriptomic–proteomic concordance highlights multicellular dysfunction in the choroid plexus in AD dementia

To determine whether cell type–specific transcriptomic changes are mirrored at the protein level, we compared snRNA-seq–derived differential gene signatures (ADd vs. NCI) across major cell types with bulk CP proteomic profiles (Fig. 5j, Extended Data Table 28). BAM cells showed strong immune activation, including enrichment of antigen presentation, leukocyte proliferation, and inflammatory pathways, with convergent late stage elevations also detected at the protein level. Epithelial cells consistently exhibited downregulation of cilia-related pathways, which was validated by corresponding protein-level reductions in ADd. In addition, we observed widespread bidirectional remodeling of barrier- and transport-associated programs—including tight junctions, extracellular matrix, cell adhesion, and ion/transport channels—spanning fibroblast, endothelial, mural, and epithelial compartments. These transcriptomic differences were likewise reflected in local stage-dependent proteomic remodeling. Together, these findings highlight three convergent signatures of CP dysfunction during AD progression: BAM immune activation, broad bidirectional remodeling of junctional, adhesion, ECM, and transport pathways, and cilia reduction.

Inferred intercellular communication changes in the choroid plexus in AD dementia

To assess differences in intercellular signaling, we applied CellChat[24] to snRNA-seq data to infer ligand–receptor–mediated communication. ADd cases showed higher weights of interactions compared with controls (Fig. 6a, number of interactions: Extended data Fig 5a). These increases were largely driven by differences in communication among fibroblasts, endothelial, immune, and mural cells through ECM-related pathways, including Collagen, Laminin, BMP, JAM, EPHA, and FN1 (Fig. 6b, Extended data Fig 5b-d, and Table 29).

Because the CP is organized into stromal, vascular, and epithelial compartments, spatial context is essential for interpreting AD-related differences. We therefore performed nearest-neighbor analysis on spatial transcriptomics data to define local microenvironments ("niches"). Each neighborhood matrix was constructed by averaging expression across a random 10-cell subset of the 25 nearest neighbors, which revealed three spatial niches (Fig. 6c-d, Extended data Fig. 6a-d): niche 1 corresponded to vessel-rich stroma (fibroblasts, endothelial, mural cells), niche 3 was enriched for epithelial cells, and niche 2 represented an intermediate epithelial environment (Extended data Fig. 6e). Spatial mapping confirmed this organization, with niche 1 localized near vessels and niche 3 closer to the epithelium, which also showed the highest expression of *TTR* (Fig. 6e-f; Extended data Fig. 6f). Examination of subtype distributions across niches revealed niche-specific enrichment of certain immune, fibroblast, and epithelial subtypes (Extended data Fig. 6g). Gene set enrichment reflected these differences: niche 1 was enriched for immune activation, inflammation, vasculature, and ECM remodeling, while niche 3 was associated with metabolism, oxidative stress, autophagy, transport, and cilia (Fig. 6h).

We next applied CellChat analysis to the spatial transcriptomic data to resolve AD-associated signaling alterations across all cells and within defined spatial niches. Consistent with single-nucleus findings, overall cell–cell communication probabilities were higher in AD, particularly within niche 3 (Fig. 6g; Extended data Fig. 6h). Across niches, the most upregulated pathways in AD involved APP-, APOE-, and ECM-related signaling (e.g., COLLAGEN, LAMININ, FN1, THBS), immune/inflammatory (MIF, CXCL), as well as growth factor–mediated networks (FGF, VEGF, PDGF, ADGRG), indicating widespread matrix remodeling and paracrine activation (Fig. 6i; Extended data Table 29). At the cell-type level, niche 1 and niche 2 showed more limited pathway activation, with significantly elevated pathways generally involving one or two dominant cell types (Fig. 6j). In contrast, niche 3 exhibited broader pathway activation that frequently involved multiple cell types (Fig. 6j), highlighting its role as a multicellular signaling hub in AD.

Discussion

By integrating single-nucleus RNA-seq, ATAC-seq and spatial transcriptomic data, we establish a multi-omic atlas for a previously understudied brain border tissue—the human choroid plexus (CP). We defined 17 distinct CP cell states and revealed their molecular remodeling across the disease continuum from normal cognition to AD dementia. Together with proteomic datasets from CP tissue and cerebrospinal fluid, these results provide a publicly accessible, multidimensional resource for investigating CP biology, barrier regulation, and disease-associated remodeling in AD and human aging. Our multi-omic analyses revealed that AD dementia was not characterized by major differences in cell-type composition but by widespread cell-intrinsic transitions that collectively reshaped the CP's immune, barrier, and stromal networks. These transitions converged into three major phenotypic axes —immune activation, barrier disruption, and stromal remodeling—that together define a chronically stressed and progressively compromised CP landscape in AD.

Along the inflammatory axis, both epithelial cells and border-associated macrophages (BAMs) exhibited progressive inflammatory activation and upregulated T-cell-activation, antigen-presentation, and cytokine-response programs, indicating coordinated immune engagement within the CP. At the late stage, BAMs apparently acquired stress-associated states marked by heat-shock-gene expression, suggesting maladaptive persistence under chronic inflammatory pressure. Consistent with these transcriptomic changes, immunostaining revealed increased $CD68^+$ and $HLA\text{-}DR^+$ macrophages indicating enhanced local macrophage activation. Despite macrophage upregulation of leukocyte-adhesion and antigen-presentation genes, we observed no change in $CD3^+$ T cells—consistent with a sustained but compartmentalized inflammatory response distinct from the leukocyte trafficking phenotype characteristic of acute injury or infection[7,24,25].

At the barrier level, our analyses revealed broad compromise of cell-junction and adhesion pathways across epithelial, endothelial, and fibroblast compartments. Epithelial cells showed selective downregulation of the tight-junction gene *CLDN5*, while pathway analyses indicated weakening of junctional integrity in secretory epithelial subtypes and endothelial cells, along with a reduction of the Mural_3 pericyte subtype, suggesting progressive loss of vascular support. In addition, fibroblasts—including the putative base-barrier Fibro_2 population—displayed lower expression of junctional components, supporting their contribution to barrier maintenance at the stromal–CSF interface. These multicellular alterations were accompanied by aberrant transporter and secretory pathways in epithelial cells along with a marked reduction in cilia function, validated by CROCC immunostaining, indicating impaired mechanosensory feedback control. Because motile and primary cilia help maintain epithelial polarity and barrier regulation through CSF sensing, their loss likely contributes to barrier dysfunction in AD. Consistent with these molecular and structural changes, CSF proteomic profiles revealed elevated inflammatory proteins together with reduced metabolic and ciliary-associated components, reflecting disrupted epithelial function and altered CSF composition in AD.

Finally, the remodeling axis highlighted bidirectional extracellular-matrix (ECM) dynamics, reflecting both matrix degradation and restrained fibrotic deposition. Fibroblasts in AD displayed mixed transcriptional signatures of cell–matrix adhesion and collagen-containing ECM organization. Movat staining showed only a mild increase in collagen accumulation, contrasting sharply with the fibrotic scarring and persistent collagen deposition typical of acute injury or infection[26–28]. Other barrier-associated compartments—including epithelial, endothelial, and mural cells—also exhibited aberrant cell–matrix adhesion and extracellular-matrix pathways (Fig. 5j; Fig.6i), consistent with a coordinated structural remodeling rather than fibroblast-specific collagen deposition. These molecular alterations were further supported by proteomic analyses of CP tissue, which revealed parallel changes in ECM-related and adhesion proteins (Fig. 5j). Thus, the CP in AD exhibited a chronic, low-grade remodeling phenotype consistent with a long-term imbalance between matrix synthesis and degradation.

Taken together, these axes define a unified model of CP dysfunction in Alzheimer's disease, characterized by chronic immune activation, barrier instability with CSF dysregulation, coordinated ECM and tissue remodeling. The coordinated transcriptional changes across epithelial, stromal, vascular, and immune compartments establish a foundation for mechanistic studies linking cilia function, chronic inflammation, and ECM turnover to disrupted CSF homeostasis. Collectively, these findings position the choroid plexus as a dynamic immune–barrier interface in AD, and highlight epithelial cilia maintenance, junctional resilience, and macrophage stress adaptation as conceptual entry points for therapeutic exploration.

Acknowledgments

We are grateful to those who agreed to donate their brains for research. We thank all the employees at RADC for their support and assistance. This study was supported by NIA grants R01AG074082 and R01AG079223 (to Y.W.) and P30AG10161, P30AG72975, R01AG015819 R01AG017917, and U01AG61356 (to D. A. B.)

Authors' contributions

D.R.A., N.A.K., and S.D.T. designed and optimized snRNA-seq and snATAC-seq. D.R.A. and S.D.T. performed sample preparation and snRNA-seq and snATAC-seq experiments. S.D.T., H.V., and D.R.A conducted spatial transcriptomics (ST) experiments. J.X. performed snRNA-seq and ATAC-seq data pre-processing. T.J.P. performed all snRNA-seq and snATAC-seq data analyses and generated related figures. T.J.P. Performed ST data preprocessing. T.J.P. and D.R.A. conducted ST analyses and generated related figures. N.A.K. contributed to snRNA-seq analyses. H.V., D.S., A.K.L., and N.A.K. performed immunohistochemistry experiments and data analysis. D.D. and N.T.S. generated mass spectrometry proteomics data. B.N. conducted proteomics analysis. T.J.P., D.R.A., and Y.W. wrote the manuscript with input from all co-authors. D.A.B. directed the parent ROSMAP study. Y.W. conceived and supervised the overall project.

Competing interests

The authors declare no competing interests.

Corresponding authors

Correspondence to Yanling Wang (yanling_wang@rush.edu)

Data availability

Sample information, cluster maker genes, and differentially expressed genes are provided in the Supplemental Information. All snRNA-seq, snATAC-seq and spatial transcriptomic data are available at Synapse under accession code syn2580853. ROS/MAP data can be requested by qualified investigators (www.radc.rush.edu).

Code availability

Code for analysis is available at GitHub (https://github.com/Tristan-J-Philippe/Multi-omic_Choroid-Plexus_Alzheimers-Disease).

426 **Online Methods**

427 **Tissue collection**

428 Human post-mortem choroid plexus (CP) tissue was collected from the lateral ventricles of 69 participants in
429 the Religious Order Study Rush Memory and Aging Project (ROSMAP)[16]. The tissue was bisected and
430 preserved for snRNA-seq, proteomics, IHC, or spatial transcriptomics. Tissue used for snRNA-seq and
431 proteomics was snap frozen and stored at -80°C whereas tissue for immunostaining and spatial transcriptomics
432 was formalin fixed and paraffin embedded. Clinical diagnostic, pathologic AD and cerebral amyloid angiopathy
433 (CCA) were assessed as previously described[16,29–31]. The Institutional Review Board of Rush University
434 Medical Center approved both studies. All participants signed an informed consent and Anatomic Gift Act.
435

436 **Nuclei isolation for snRNA-seq**

437 The clinical diagnosis was used to group ADd, MCI, and NCI into batches of 4-6 participants for snRNA-seq
438 (n=69; Fig.1b, Extended Data Table 1); these groups were balanced for age and sex. All procedures were
439 carried out on ice or at 4 °C to minimize RNA degradation, unless otherwise specified. 100 mg frozen CP tissue
440 was minced on dry ice, then thawed in 0.1X lysis buffer (250 mM sucrose, 25 mM KCl, 5 mM MgCl2, 10 mM
441 Tris pH8, 1µM DTT, 15µM actinomycin, 0.2U/µL RNAse inhibitor, 0.01% v/v Triton X-100). Tissue was
442 pressed through a 100µm cell strainer with the back end of a 5mL plunger, rinsing every 30 seconds with 200
443 µL fresh 0.1X lysis buffer for 3 min total per sample. The cell suspension was pelleted at 600g for 4 min (all
444 centrifugation steps were at 4°C), supernatant was removed, and pellets were resuspended in 1.5 mL 1X lysis
445 buffer with 0.1% Triton X-100. Nuclei were homogenized using a Dounce homogenizer (10 times using pestle
446 B) and incubated for 2 min on ice. Nuclei were washed twice: centrifuged at 700g for 4 min and resuspended in
447 1 mL of wash buffer (1.5% BSA, 0.2U/µL RNAse inhibitor in DPBS). Samples were purified by iodixanol
448 gradient (37%, 29%, 25% with sample) centrifugation (13500g, 20min, OptiPrep Sigma) and collected from the
449 29-37% interface, washed once, filtered through a 40 µm cell strainer (Flowmi), and washed again before QC
450 and counting using Trypan blue.
451

452 For barcoding, nuclei (100k in 187.5uL total volume * 2 unique barcodes per sample) were incubated with 4
453 µM of anchor and 4 µM of a unique barcoded oligonucleotide and incubated for 5min (final concentration of 50
454 nM of each; see Nuclei hashing design). Followed by 4 µM co-anchor, mixed by tapping, incubated on ice for 5
455 min, and 3 washes. Hashed nuclei were then combined, diluted to ~40k nuclei in 43.2 µL, and super-loaded
456 (~40k nuclei loaded per lane) onto 4 lanes of 10X Genomics Chip G or Chip J. Libraries were prepared using
457 the 10x Genomics 3' single-cell gene expression assay v3.1 (CG000317 Rev C) for snRNA-seq alone and
458 (CG000338) for single nuclei RNA and ATAC sequencing except as detailed in method: Nuclei hashtag,

459 followed by sequencing on a NovaSeq 6000 to an average read depth of 50k RNA reads/cell and 15k hash
460 reads/cell.
461
462 **Nuclei hashtag oligonucleotide design and library preparation**
463 Nuclei were barcoded using a modified MULTI-seq[32] protocol to enable pooling and super-loading of the 10X
464 chip. The Anchor sequence was: /5Chol-
465 TEG/GTAACGATCCAGCTGTCACTAGATCGGAAGAGCACACGTCTG, where '5Chol-TEG' denotes a 5'
466 Cholesterol modification conjugated via a triethylene glycol linker. The Co-Anchor sequence was:
467 AGTGACAGCTGGATCGTTAC/3CholTEG/. Sixteen barcoded oligonucleotides (aka "hashtag oligos") were
468 designed following the pattern R2-BC-poly(A), where R2 was a constant partial Read 2 sequence
469 (CAGACGTGTGCTCTTCCGATCT), BC was a unique sample-specific 15-nt barcode sequence (sequences
470 listed below), and poly(A) was a 30-nt poly(A) sequence. The poly(A) enables recovery of hashtag oligos along
471 with mRNA following reverse transcription. To further enrich for hashtag oligos, a Truseq 2 primer
472 (CAGACGTGTGCTCTTCCGATC) was spiked into the cDNA amplification reaction (CG000317 Rev C step
473 2.2) at 100 nM. All oligonucleotides were ordered from IDT. For the hashtag library sample index PCR (step
474 3.5), the reaction consisted of 50 µl Amp mix, 40 µl EB buffer, 5 µl cDNA from transferred supernatant
475 cleanup (step 2.3B), and 5 µl dual index from plate TT. PCR was run for 9 cycles with default settings,
476 followed by a 1.2X SPRI cleanup. Next, 20 ng (~1 µl) of PCR product was used for an additional sample index
477 PCR (6 cycles) to enrich for full-length product. The reaction also consisted of 30 µl Amp mix, 1.2 µl each of
478 Illumina P5 and P7 primers (10 µM), and EB buffer to a total volume of 60 µl. This was followed by one 0.9X
479 SPRI cleanup to remove free primer and primer dimer. The hashtag (HT) libraries (~242-bp total size) were
480 mixed with GEX libraries (ensuring distinct TT indices) at a molar ratio of 1:6 HT:GEX in the final pool to
481 achieve the desired ~1:3 ratio of sequencing reads.
482 Sample barcodes:
483 AAGGCAGACGGTGCA
484 GGCTGCGCACCGCCT
485 GACGCGCGTTGTCAT
486 GAAGAAGCGTTATTC
487 AGAGCTAGGATCGGA
488 GCTAGCGTAATGTGG
489 CGGTTAGCGCGGTTC
490 AGGCGTGCACGTGGT
491 CACATATAGAATTAG
492 ATAGCGGCTCTATCG
493 AGCGCATAGTTATCT

494 CAGGTCGGCCAAGAT
495 GCCAAGATCAGGTCC
496 TAGGTTACGAGTGTG
497 ATAATCATTACGTGG
498 ATCGAACCGACAGAG
499
500 **Spatial transcriptomics of CP using Nanostring CosMx**
501 Eight human CP samples were selected (4 NCI, 4 AD), matched for sex, and balanced for age. 5-µm thick FFPE
502 sections were mounted on Leica BOND Plus microscope slides (4 sections per slide; 2 slides total), ensuring
503 that the tissue resided within the 15x20mm imaging area. Slide preparation followed the manufacturer's
504 protocol (Nanostring MAN10159-03) with the following modifications. Antigen retrieval was carried out using
505 a steamer for 15 min once the retrieval solution reached 99°C. Tissue permeabilization was performed for 15
506 min at 40°C using 3 µg/mL Proteinase K. Probe hybridization occurred for 18 hr at 37°C.
507
508 Primary antibodies included Cell Segmentation Mix 1 (CD298/B2M), Marker Mix 1 (PanCK/CD45), and
509 Marker Mix 2 (CD68) at the recommended dilutions and were incubated for 90 min (instead of 60 min) at room
510 temperature. To load slides on the Nanostring CosMx instrument, we followed the Instrument User Manual
511 (MAN-10161-03-2; software version 1.2) using configuration B for pre-bleaching and configuration A for cell
512 segmentation. Field of view (FOV) selection encompassed the entire tissue-covered area.
513
514 **TMT-based proteomics of choroid plexus tissue**
515 A subset of choroid plexus samples (n = 16; Extended Data Table 1), balanced for age and sex, were analyzed
516 by mass spectrometry. Briefly, tissues were lysed in 8 M urea, 100 mM Tris, 100 mM NaH_2PO_4 (pH 8.5) with
517 protease and phosphatase inhibitors (Thermo Fisher), reduced with 5 mM dithiothreitol, alkylated with 10 mM
518 iodoacetamide, and digested overnight with trypsin. Peptides were labeled using the TMTpro 16-plex kit
519 (Thermo Fisher Scientific), pooled, and fractionated by high-pH reversed-phase chromatography. Fractions
520 were analyzed on an Orbitrap Lumos mass spectrometer (Thermo Fisher Scientific) coupled to a 3000 RSLC
521 nano-UPLC system using a 26-min gradient on a 1.7 µm C18 column (Waters). MS scans were acquired at
522 120,000 resolution with a 3 s cycle time, and the top precursors (charge 2–5) were selected for MS/MS with
523 higher-energy collisional dissociation (HCD 35%), 50,000 resolution, 125k AGC target, and 86 ms maximum
524 injection time, with dynamic exclusion of 20 s. Raw files were processed in Proteome Discoverer v3.0 using
525 Sequest HT against the UniProt human proteome database for TMT-based quantification, and protein
526 abundances were normalized across channels for downstream analysis.
527
528 **Olink-based proteomics of cerebrospinal fluid**

529 Cerebrospinal fluid (CSF) samples (n=24; Extended Data Table 1) were analyzed using the Olink Explore 384
530 platform (Thermo Fisher Scientific). The following panels were included: Cardiometabolic, Cardiometabolic II,
531 Inflammation, Inflammation II, Neurology, Neurology II, Oncology, and Oncology II. Data processing, QC,
532 and normalization were performed using the Explore Calculation Module v3.8.1, applying intensity
533 normalization on a $\log_2$ scale.
534
535 **snRNA-seq**
536 We ran bcl2fastq, followed by CellRanger v7.0.1 to generate RNA, ATAC, and hash count matrices using the
537 GRCh38 genome. Downstream analyses were conducted in R Seurat v4.2.0 package[33]. RNA and ATAC count
538 matrices were treated separately to retain nuclei with sufficient modality-specific quality. For snRNA-seq we
539 excluded droplets with >12,000 or <500 features and <500 counts. Ambient RNA contamination was corrected
540 using SoupX v1.6.2[34] with autoEstCont (tfidfMin=0.7–0.9) to ensure at least 100 genes were used for estimation.
541 Nuclei were demultiplexed using HTOdemux, which also flagged hash doublets.
542
543 In alignment with previously established strategies for guided doublet removal[35,36] we leveraged previously
544 reported markers for the choroid plexus, brain vasculature, and brain immune cells in mouse and human (see
545 Extended Data Table 30). Data were normalized and scaled incorporating the top 3k variable features and
546 reported markers, which were then used for Principal Component Analysis (PCA, top 30 embeddings),
547 Harmony[37] v0.1.0 integration by sequencing library, dimensionality reduction (UMAP), and clustering
548 (Louvain algorithm, res=0.03-0.7)[38]. Positive marker genes were identified using a bimodal Wilcox rank sum-
549 test ($\log_2$FC>0.25, p<0.05). Since 'dark' epithelial cells are characterized by high mitochondrial content[39,40],
550 mitochondrial content >5% were only retained in the epithelial cluster. Nuclei with mixed cluster signatures
551 were excluded, known doublets were removed and misclustered cells were removed from UMAP plots. Data
552 were iteratively reprocessed as above but in an unsupervised manner with the top 3k unknown variable features
553 to identify major and sub cell types.
554
555 **snATAC-seq**
556 Following the generation of raw count matrices, we utilized Seurat v4.2.0[33] and Signac 1.10.0[41] . Low-quality
557 droplets with total fragments <100 or >5,000, blacklist ratio >0.1, nucleosome signal >4, and transcription start
558 site (TSS) enrichment score <3 was excluded. After demultiplexing with HTODemux, doublets were removed
559 using the semi-supervised method described above (Methods: snRNA-seq). Chromatin accessibility data were
560 normalized using RunTFIDF, reduced with RunSVD, and the top 30 components were used for dimensionality
561 reduction and clustering. To annotate clusters, we generated a pseudo-expression "activity" matrix, which was
562 normalized, scaled and a bimodal Wilcoxon rank-sum test ($\log_2$FC > 0.25, p<0.05) was used to identify cell
563 type markers. We annotated chromatin features with the UCSC Genome Browser, motif analysis with

motifmatchR v1.31.1[42] (JASPAR 2022, default thresholds), and transcription factor activity with Signac Footprint (default settings).

Spatial transcriptomics

Initial preprocessing followed the AtoMx pipeline (MAN-10162-03; software v1.2). Cellpose v2 was used for segmentation (non-neuro human tissue, cell dilation: 2.17 µm, cell diameter: 7.28 µm, nucleus size: 7.2 µm, membrane size: 5.7µm, Models: cyto2, flow threshold: 0.1, probability threshold: 2, min. size: 3.6µm) followed by QC and flat file export to Seurat v5.1.0[43]. Segmented cells with <100 counts, >3500 counts, <50 features, >2000 features, qcCellsFlagged==T, or an area <10µm^2 were excluded. We used SCTransform v.0.4.1[44,45]to correct, scale, and normalize; and harmony to correct for individual and slide effects. The semi-supervised method described above (Methods: snRNA-seq) was used to identify potential segmentation errors (e.g. cells with high expression of marker genes from multiple major cell types). These were excluded for downstream cell type annotation (unsupervised, top 2k) and AD-differential testing but retained for spatial neighborhood and CellChat analysis. Due to limitations of unsupervised clustering algorithms in resolving rare cell types (<6,000 cells per major cell type), we applied a supervised mapping approach using the snRNA-seq dataset as reference. Specifically, spatial transcriptomics data were annotated using RCTD[23] with default parameters, leveraging pseudobulked snRNA-seq expression profiles for each major cell type as reference.

Differential expression analyses

We performed differential gene expression, protein abundance, and chromatin accessibility analyses using a linear modeling framework with empirical Bayes moderation as implemented in voom and limma v3.54[46]. Where applicable, models were adjusted for age, sex, postmortem interval (PMI), and sequencing library. Genes and proteins with fewer than two counts per sample or expressed in fewer than 1% of cells were excluded. Accessible chromatin regions and gene activity scores with variance-standardized transformation (vst) scores below 1 were removed. For the snRNA-seq dataset, samples with >100,000 total pseudobulked counts were split by sequencing library to create technical replicates; samples with <60,000 counts were excluded. Genes with a false discovery rate (FDR) <0.01 and absolute log2 fold change (LFC) >0.5 were considered differentially expressed. For smaller datasets (spatial transcriptomics, chromatin accessibility (snATAC-seq), and proteomics) validation thresholds were relaxed ($p < 0.05$, $LFC > 0.2$). We tested cell type specific transcriptional signatures and correlated these between modalities. We tested contrasts between clinical diagnostic (cogdx), neuropathological categories (adnc_ad), and cognitive decline (last cognitive score before death) among major and minor cell types.

Enrichment analysis

598 Ranked gene lists were stratified by directionality and tested using fgsea v1.25[47] against Gene Ontology (GO)
599 Biological Process, Molecular Function, and Cellular Component pathways. A normalized enrichment score
600 (NES) >0.6 and FDR <0.01 for snRNA-seq and FDR<0.15 for spatial transcriptomics, snATAC-seq, and
601 proteomics were used to define significant pathways. Enrichment and differential expression results were
602 visualized using ClueGO v2.5.10[48], Cytoscape v3.10.2, ComplexHeatmap[49,50], Seurat, and ggplot2 v3.4.4[51].
603

604 **Proportion analysis**

605 As previously described[52], we applied a linear modeling with empirical Bayes moderation to assess cell type
606 proportions as a function of cognitive diagnosis (cogdx). Where applicable, models were adjusted for
607 parenchymal contamination, age, sex, and PMI. Statistical significance was defined as FDR < 0.01.
608

609 **Pattern matching in snRNA-seq**

610 We applied a template matching algorithm[22] to identify genes associated with disease progression along three
611 possible positive and negative trajectories. Differentially expressed genes (p<0.05, LFC>0.25) from the MCI vs.
612 NCI, ADd vs. MCI, and ADd vs. NCI contrasts were classified as early-stage (significant in MCI vs. NCI and
613 ADd vs. MCI, but not AD vs. NCI), late-stage (significant in ADd vs. MCI and ADd vs. NCI, but not MCI vs.
614 NCI), and progressive (significant in MCI vs. NCI and ADd vs. NCI) patterns. Genes were correlated with the
615 corresponding stage template, and only those with p < 0.05 were retained.
616

617 **Nearest Neighbor analysis**

618 To obtain a better understanding of cell-cell interaction we included cells with mixed signatures and mapped
619 cells to their closest major cell type (Methods: Spatial transcriptomics data processing), only excluding cells
620 that did not meet QC metrics, parenchymal cells and red blood cells. This resulted in 166,607 total cells for
621 analysis. A spatial neighborhood matrix was generated using CellularNeighborhoods v0.0.0.9000 available
622 here: https://github.com/Nanostring-Biostats/CosMx-Analysis-Scratch-Space/tree/Main/_code/cellular-
623 neighborhoods. Each cell's neighborhood expression was calculated as the mean expression of a random 10-cell
624 subset of its 25 nearest neighbors, based on cell centroid x-y coordinates. We performed normalization/scaling,
625 PCA (50 components), Harmony (50 components, accounting for slide batch, individual, and AD status),
626 UMAP, and clustering (kmeans = 3) to obtain 3 spatial neighborhoods or 'niches'.
627

628 **CellChat**

629 We used CellChat v1.6.1[24] to infer intercellular communication networks among major cell types stratified per
630 cognitive diagnosis (MCI, MCI, and ADd) with default parameters for the snRNA-seq dataset and for spatial
631 transcriptomics after nearest neighbor analysis. For spatial transcriptomics, CellChat was run separately for
632 each niche with SCTransformed counts, computeCommunProb with a contact.range=20 microns,

633 interaction.range=250 microns, scale.distance=0.69 (empirically determined), and all other parameters default.
634 We also normalized cellchat metrics (interaction weight, net$prob, netP$prob, and centrality score) by the
635 number of cell pairs with the potential for interaction (e.g. within 250 microns), thereby accounting for
636 differences in cell number and density between NCI and AD, as well as across niches.
637
638 To identify disease-associated signaling pathways, objects for each cognitive diagnosis were merged and
639 comparative network analyses performed. A customrankNet() function was implemented to rank pathways with
640 $p<0.05$ by summed communication probability (weight) per condition, calculating relative contributions across
641 diagnostic groups. Pathway-level metrics (information flow and interaction counts) were extracted from the
642 netP slot of the merged object. To assess cell-type-specific signaling changes, centrality scores (incoming +
643 outgoing) were computed for each cell type and condition using netAnalysis_computeCentrality(). To ensure
644 robust conclusions, previously identified (Methods: Differential analyses: Expression) statistics for each ligand-
645 receptor pair were utilized and the average $\log_2$FC of ligand and receptor(s) was calculated. We removed non-
646 directional or low-confidence interactions (ligand-receptor pairs with absolute combined $\log_2$FC < 0.05, ligand
647 detected in < 5% of sender cells, receptor detected in < 5% of receiver cells, and/or net$p > 0.05). At the
648 pathway level, median $\log_2$FC was calculated per pathway and a Wilcoxon signed-ranked test was applied to
649 pathways with ≥ 3 interactions followed by FDR correction. Pathways defined as significant had absolute
650 median $\log_2$FC ≥ 0.15, FDR ≤ 0.01, absolute AD-differential net centrality > 0.0001, and matched centrality and
651 median $\log_2$FC directionality.
652
653 **Cell-cell distance-based analysis**
654 We converted centroid x-y coordinates from pixels to microns (x0.18) and computed per-cell distances to the
655 nearest cell type (e.g. Mural/Endothelial, Epithelial, Parenchymal), then calculated and plotted per-individual
656 averages across spatial niches or cell subtypes. We performed a Kruskal-Wallis test and used Dunn's test with
657 Benjamini-Hochberg correction for multiple testing.
658
659 **Immunohistochemistry**
660 Human FFPE CP sections were stained using a Bond-Rx research stainer (Leica Biosystems). Briefly, slides
661 were baked for 60 min at 60°C prior to dewaxing for 30 s at 72°C. For multiplexed cell typing, an Opal 6-plex
662 detection kit (Akoya Biosciences #NEL871001KT) was used as follows; slides were incubated with CD45
663 (1:50) for 30 min followed by 10 min Opal polymer HRP Ms+Rb and 10 min Opal signal development with
664 Opal 620 diluted at 1:150. Slides were antigen retrieved for 20 min in pH 6.0 citrate buffer solution (Leica
665 Biosystems #AR9961) and the process was repeated with DCN (1:100; Opal 570 (1:150)), TTR (1:500; Opal
666 690 (1:150)), PECAM (1:50; Opal 520 (1:150)) and ACTA2 (1:1000; Opal 480 (1:150)). For ciliary rootlet
667 structures, slides were subjected to HIER with a pH 9.0 EDTA buffer solution (Leica Biosystems #AR9640) for

668 20 min at 100°C followed by 10 min peroxide block. CROCC (1:100) and TTR (1:500) were incubated together
669 for 60 minutes followed by 60 min of secondary anti-rabbit Alexa Fluor 647 (1:1000) for CROCC. The TTR
670 antibody was detected with a Mouse IgG-HRP secondary, incubated for 60 min, followed by a 5 min incubation
671 with TSA Fluorescein. All slides were then incubated with Trueblack quencher for 1 minute, counter stained
672 with spectral DAPI for 5 min, and mounted. Imaging was performed using a PhenoImager (Akoya Biosciences)
673 at 40X. ROIs were selected using Phenochart 2.2.0 (Akoya Biosciences) and spectrally unmixed composite
674 TIFs were generated using inForm (Akoya Biosciences).
675
676 For CROCC puncta analysis, images were imported into ImageJ and split into individual channels. CROCC
677 channel image was converted into 8-bit and threshold was set to mask only the puncta. Analyze particles tool in
678 ImageJ was run with the following parameters: Size=1.5-25.0 µm and Circularity= 0.1-1.0. The results were
679 exported and analyzed in GraphPad prism (v10.5.0). For classification of TTR+ epithelial cells, the raw
680 composite TIFs were analyzed using Qupath (v0.5). Cells were defined in each ROI using QuPath Cell
681 Detection tool with the following parameters, requested pixel size = 0.5µm, background radius = 8µm, median
682 filter radius =0µm, Sigma value for Gaussian filter = 1.5µm, minimum nucleus area = 10µm^2, maximum
683 nucleus area =400µm^2, and intensity threshold = 2. Cell parameters include a cell expansion of 5µm from the
684 cell nucleus, and general parameters include smoothing of the detected nucleus/cell boundaries. Shape, intensity
685 and smoothing features were added for all detections, and the "Train object classifier" tool was used to classify
686 the TTR+ epithelial cells. All measurements were exported and analyzed in GraphPad prism (v10.5.0).
687
688 **Multiplex immunohistochemical staining using Akoya Phenocycler fusion (PCF)**
689 Human FFPE CP sections were stained using the Akoya Biosciences Phenocycler Fusion 2.0 workflow as per
690 manufacturer's instructions. Briefly, the slides were baked overnight at 60 degrees and de-waxed, hydrated and
691 antigen retrieval performed in a pressure cooker for 20 min in AR9 buffer. Staining was performed for 3 hrs at
692 room temperature followed by washing and post-fixation steps. Imaging was performed on Akoya Phenocycler
693 Fusion 2.0 instrument at 20X. Qptiff image files generated were imported into QuPath (v0.5) for quantitative
694 analysis.
695
696 **Phenocycler Fusion Image Analysis**
697 For analysis of CD163+ BAM cells, ROIs were defined in each image and QuPath Cell Detection tool was used
698 with following parameters: detection channel= CD163, requested pixel size = 0.5µm, background radius =
699 20µm, median filter radius =0µm, Sigma value for Gaussian filter = 1.5µm, minimum nucleus area = 15µm^2,
700 maximum nucleus area =400µm^2, and intensity threshold = 50. No cell parameters were selected, and general
701 parameters include smoothing of the detected nucleus/cell boundaries. HLA-DR and CD68 intensity
702 measurements from CD163$^+$ cells were exported and analyzed in GraphPad Prism (v10.5.0).

703

704 For T-cell analysis, ROIs were defined in each image and QuPath Cell Detection tool was used with following
705 parameters: detection channel= CD3e, requested pixel size = 0.5µm, background radius = 20µm, median filter
706 radius =0µm, Sigma value for Gaussian filter = 1.5µm, minimum nucleus area = 10µm^2, maximum nucleus area
707 =400µm^2, and intensity threshold = 50. No cell parameters were selected, and general parameters include
708 smoothing of the detected nucleus/cell boundaries. Shape, intensity and smoothing features were added for all
709 detections, and the "Train object classifier" tool was used to classify the CD4+ and CD8+ T-cells. All T-cells
710 were manually annotated based on whether they are present inside (non-infiltrating) or outside (infiltrating) of
711 Caveolin/Collagen IV+ vessels. The numbers of infiltrated T cells were plotted relative to the area of the ROIs
712 and analyzed in GraphPad Prism (v10.5.0).

713

714 **Movat's Pentachrome staining and analysis**

715 Human FFPE CP sections were stained with Movat's Pentachrome stain kit (Abcam, ab245884) as per the
716 manufacturer's instructions in two batches. Slides were imaged using the Phenocycler Imaging system (Akoya
717 Biosciences) at 40X. 4-10 ROIs (928µm x 697µm) were selected from each case using Akoya Phenochart 2.2.0
718 and RGB TIFs were exported using inForm (Akoya Biosciences).
719 Images were processed using the Colour Deconvolution Package (https://blog.bham.ac.uk/intellimic/g-landini-
720 software/colour-deconvolution-2/) in ImageJ (v1.54) to extract the yellow channel. Images were converted to 8
721 bit and exported as image txt files for further processing in R. Background subtraction was performed to align
722 batches, and pixels that did not correspond to tissue were excluded. For each ROI, the distribution of pixel
723 intensities was calculated. The pixel distributions for each individual were averaged to present the distribution
724 for each disease group, plotted with ggplot2. The AUC for each ROI at high collagen (cutoff of 200) was
725 calculated using the trapz() function from the pracma library (v2.4.4) and a one-way ANOVA performed to test
726 significance.

727

728

References

1. Saunders, N. R., Dziegielewska, K. M., Fame, R. M., Lehtinen, M. K. & Liddelow, S. A. The choroid plexus: a missing link in our understanding of brain development and function. *Physiol. Rev.* **103**, 919–956 (2023).
2. Verhaege, D. *et al.* Newly discovered base barrier cells provide compartmentalization of choroid plexus, brain and CSF. *bioRxiv* (2024) doi:10.1101/2024.07.08.601696.
3. Gião, T., Teixeira, T., Almeida, M. R. & Cardoso, I. Choroid plexus in Alzheimer's disease-the current state of knowledge. *Biomedicines* **10**, 224 (2022).
4. Rasmussen, M. K., Mestre, H. & Nedergaard, M. Fluid transport in the brain. *Physiol. Rev.* **102**, 1025–1151 (2022).
5. Attier-Zmudka, J. *et al.* Decreased cerebrospinal fluid flow is associated with cognitive deficit in elderly patients. *Front. Aging Neurosci.* **11**, 87 (2019).
6. Ferdinando, H., Moradi, S., Korhonen, V., Kiviniemi, V. & Myllylä, T. Altered cerebrovascular-CSF coupling in Alzheimer's Disease measured by functional near-infrared spectroscopy. *Sci. Rep.* **13**, 22364 (2023).
7. Xu, H. *et al.* The choroid plexus synergizes with immune cells during neuroinflammation. *Cell* **187**, 4946-4963.e17 (2024).
8. Pichet Binette, A. *et al.* Proteomic changes in Alzheimer's disease associated with progressive Aβ plaque and tau tangle pathologies. *Nat. Neurosci.* **27**, 1880–1891 (2024).
9. Shen, Y. *et al.* Systematic proteomics in Autosomal dominant Alzheimer's disease reveals decades-early changes of CSF proteins in neuronal death, and immune pathways. *medRxiv* (2024) doi:10.1101/2024.01.12.24301242.
10. Liu, R. *et al.* Choroid plexus epithelium and its role in neurological diseases. *Front. Mol. Neurosci.* **15**, 949231 (2022).
11. Stopa, E. G. *et al.* Comparative transcriptomics of choroid plexus in Alzheimer's disease, frontotemporal dementia and Huntington's disease: implications for CSF homeostasis. *Fluids Barriers CNS* **15**, 18 (2018).
12. Delvenne, A. *et al.* Involvement of the choroid plexus in Alzheimer's disease pathophysiology: findings from mouse and human proteomic studies. *Fluids Barriers CNS* **21**, 58 (2024).
13. Brkic, M. *et al.* Neurobiology of Disease. *J. Neurosci.* **35**, 12766–12778 (2015).
14. Yan, Z.-J., Ye, M., Li, J., Zhang, D.-F. & Yao, Y.-G. Early transcriptional and cellular abnormalities in choroid plexus of a mouse model of Alzheimer's disease. *Mol. Neurodegener.* **20**, 62 (2025).
15. Tijms, B. M. *et al.* Cerebrospinal fluid proteomics in patients with Alzheimer's disease reveals five molecular subtypes with distinct genetic risk profiles. *Nat. Aging* **4**, 33–47 (2024).
16. Bennett, D. A. *et al.* Religious Orders Study and Rush Memory and Aging Project. *J. Alzheimers. Dis.* **64**, S161–S189 (2018).

764 17. Kearns, N. A. *et al.* Dissecting the human leptomeninges at single-cell resolution. *Nat. Commun.* **14**, 7036
765 (2023).
766 18. Fullard, J. F. *et al.* Single-nucleus transcriptome analysis of human brain immune response in patients with
767 severe COVID-19. *Genome Med.* **13**, 118 (2021).
768 19. Yang, A. C. *et al.* Dysregulation of brain and choroid plexus cell types in severe COVID-19. *Nature* **595**,
769 565–571 (2021).
770 20. Sérot, J., Béné, M., Foliguet, B. & Faure, G. Morphological alterations of the choroid plexus in late-onset
771 Alzheimer's disease. *Acta Neuropathol.* **99**, 105–108 (2000).
772 21. Pavlidis, P. & Noble, W. S. Analysis of strain and regional variation in gene expression in mouse brain.
773 *Genome Biol.* **2**, RESEARCH0042 (2001).
774 22. Cable, D. M. *et al.* Robust decomposition of cell type mixtures in spatial transcriptomics. *Nat. Biotechnol.*
775 **40**, 517–526 (2022).
776 23. Jin, S. *et al.* Inference and analysis of cell-cell communication using CellChat. *Nat. Commun.* **12**, 1088
777 (2021).
778 24. Kunis, G. *et al.* IFN-γ-dependent activation of the brain's choroid plexus for CNS immune surveillance
779 and repair. *Brain* **136**, 3427–3440 (2013).
780 25. Reboldi, A. *et al.* C-C chemokine receptor 6-regulated entry of TH-17 cells into the CNS through the
781 choroid plexus is required for the initiation of EAE. *Nat. Immunol.* **10**, 514–523 (2009).
782 26. Fernández-Klett, F. & Priller, J. The fibrotic scar in neurological disorders. *Brain Pathol.* **24**, 404–413
783 (2014).
784 27. Xue, X. *et al.* Heterogeneous fibroblasts contribute to fibrotic scar formation after spinal cord injury in
785 mice and monkeys. *Nat. Commun.* **15**, 6321 (2024).
786 28. Dias, D. O. *et al.* Pericyte-derived fibrotic scarring is conserved across diverse central nervous system
787 lesions. *Nat. Commun.* **12**, 5501 (2021).
788 29. Bennett, D. A. *et al.* Neuropathology of older persons without cognitive impairment from two community-
789 based studies. *Neurology* **66**, 1837–1844 (2006).
790 30. Schneider, J. A., Arvanitakis, Z., Leurgans, S. E. & Bennett, D. A. The neuropathology of probable
791 Alzheimer disease and mild cognitive impairment. *Ann. Neurol.* **66**, 200–208 (2009).
792 31. Arvanitakis, Z. *et al.* Cerebral amyloid angiopathy pathology and cognitive domains in older persons. *Ann.*
793 *Neurol.* **69**, 320–327 (2011).
794 32. McGinnis, C. S. *et al.* MULTI-seq: sample multiplexing for single-cell RNA sequencing using lipid-tagged
795 indices. *Nat. Methods* **16**, 619–626 (2019).
796 33. Hao, Y. *et al.* Integrated analysis of multimodal single-cell data. *Cell* **184**, 3573-3587.e29 (2021).
797 34. Young, M. D. & Behjati, S. SoupX removes ambient RNA contamination from droplet-based single-cell
798 RNA sequencing data. *Gigascience* **9**, (2020).

35. Green, G. S. *et al.* Cellular communities reveal trajectories of brain ageing and Alzheimer's disease. *Nature* **633**, 634–645 (2024).
36. Dani, N. *et al.* A cellular and spatial map of the choroid plexus across brain ventricles and ages. *Cell* **184**, 3056-3074.e21 (2021).
37. Korsunsky, I. *et al.* Fast, sensitive and accurate integration of single-cell data with Harmony. *Nat. Methods* **16**, 1289–1296 (2019).
38. Waltman, L. & van Eck, N. J. A smart local moving algorithm for large-scale modularity-based community detection. *Eur. Phys. J. B* **86**, 6–471 (2013).
39. Garma-Aviña, A. Cytology of the normal and abnormal choroid plexi in selected domestic mammals, wildlife species, and man. *J. Vet. Diagn. Invest.* **16**, 283–292 (2004).
40. Pellegrini, L. *et al.* Human CNS barrier-forming organoids with cerebrospinal fluid production. *Science* **369**, eaaz5626 (2020).
41. Stuart, T., Srivastava, A., Madad, S., Lareau, C. A. & Satija, R. Single-cell chromatin state analysis with Signac. *Nat. Methods* **18**, 1333–1341 (2021).
42. Schep, A. *Fast Motif Matching in R*. https://bioconductor.org/packages/devel/bioc/manuals/motifmatchr/man/motifmatchr.pdf (2025).
43. Hao, Y. *et al.* Dictionary learning for integrative, multimodal and scalable single-cell analysis. *Nat. Biotechnol.* **42**, 293–304 (2024).
44. Choudhary, S. & Satija, R. Comparison and evaluation of statistical error models for scRNA-seq. *Genome Biol.* **23**, 27 (2022).
45. Hafemeister, C. & Satija, R. Normalization and variance stabilization of single-cell RNA-seq data using regularized negative binomial regression. *Genome Biol.* **20**, 296 (2019).
46. Ritchie, M. E. *et al.* limma powers differential expression analyses for RNA-sequencing and microarray studies. *Nucleic Acids Res.* **43**, e47 (2015).
47. Korotkevich, G., Sukhov, V. & Sergushichev, A. Fast gene set enrichment analysis. *bioRxiv* (2016) doi:10.1101/060012.
48. Bindea, G. *et al.* ClueGO: a Cytoscape plug-in to decipher functionally grouped gene ontology and pathway annotation networks. *Bioinformatics* **25**, 1091–1093 (2009).
49. Gu, Z., Eils, R. & Schlesner, M. Complex heatmaps reveal patterns and correlations in multidimensional genomic data. *Bioinformatics* **32**, 2847–2849 (2016).
50. Gu, Z. Complex heatmap visualization. *Imeta* **1**, e43 (2022).
51. Wickham, H. *Ggplot2: Elegant Graphics for Data Analysis*. (Springer International Publishing, Cham, Switzerland, 2016).
52. Phipson, B. *et al.* propeller: testing for differences in cell type proportions in single cell data. *Bioinformatics* **38**, 4720–4726 (2022).

Main Figures

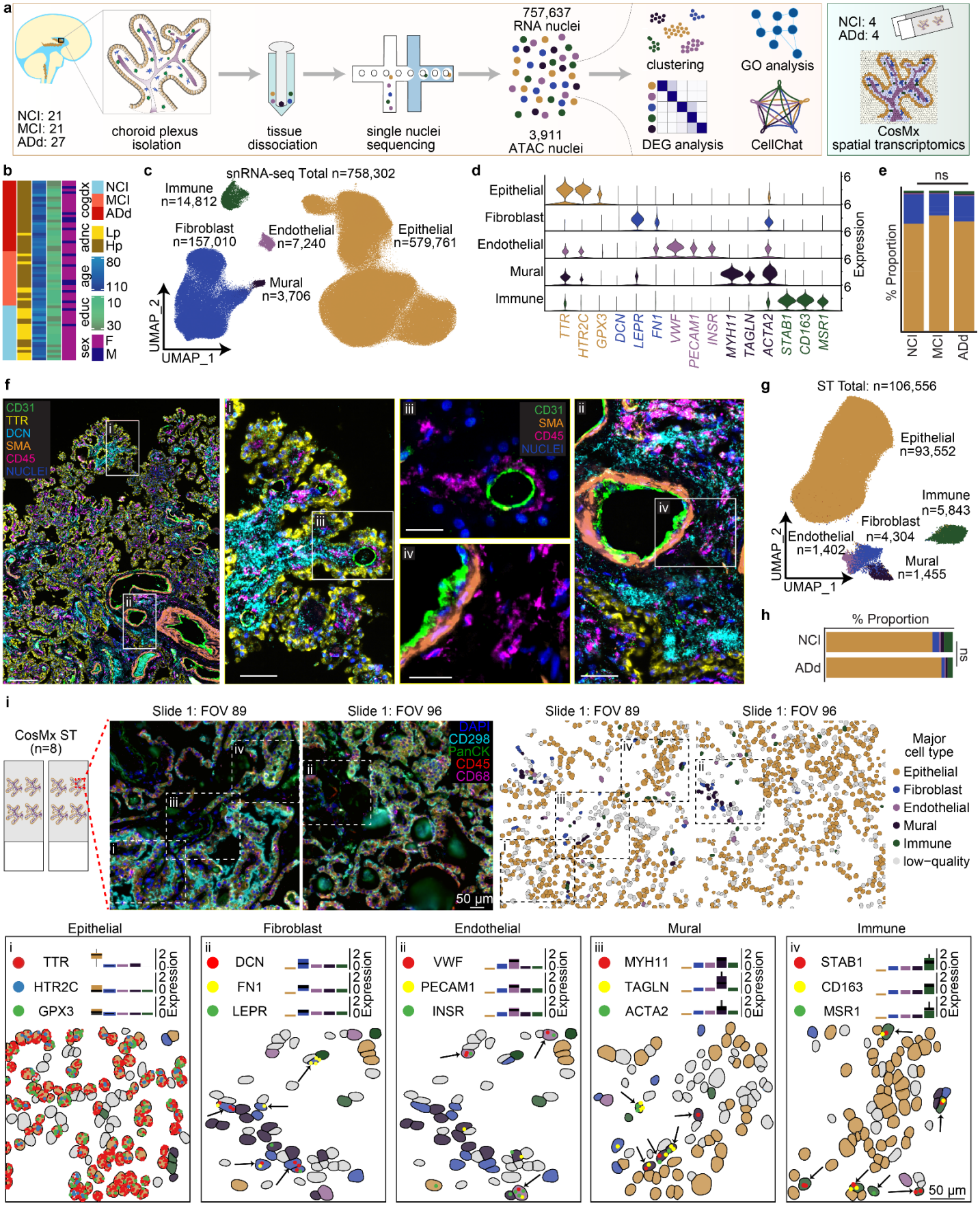

Fig. 1: Major cell classes of the human choroid plexus

a, Study design overview. snRNA-seq was performed on 69 participants (757,637 nuclei), snATAC-seq was performed on nuclei from 6 participants (3,238 nuclei), and spatial transcriptomics (ST) on 8 participants (106,556 segmented cells).

b, Participant demographics, balanced for age, sex, and education (educ). Clinical (cogdx) and neuropathological (ad_adnc) diagnoses are indicated. See Extended Data Table 1.

c, snRNA-seq UMAP colored by major cell types.

d, snRNA-seq canonical marker expression violin plot per cell cluster (FDR < 0.01, $\log_2$FC > 0.25). See Extended Data Table 2.

e, snRNA-seq major cell type proportions stratified by clinical diagnosis (all not significant, FDR > 0.01, ns).

f, Multiplexed immunohistochemistry staining for CD31, TTR, DCN, SMA, CD45 and DAPI. Scale bars = 200 µm (overview), 50 µm (i, ii) and 20 µm (iii, iv).

g, Unsupervised spatial transcriptomics (ST) UMAP projection of major cell types.

h, Proportion of epithelial subclusters in ST data.

i, Adjacent spatial transcriptomics fields of view (FOVs #1.89 and #1.96) Upper left: immunostaining. Upper right: segmented cells colored by major cell type. Below: transcript localization with quantified expression (upper) and example FOV (lower). Arrows indicate marker localization. Scale bars, 50 µm.

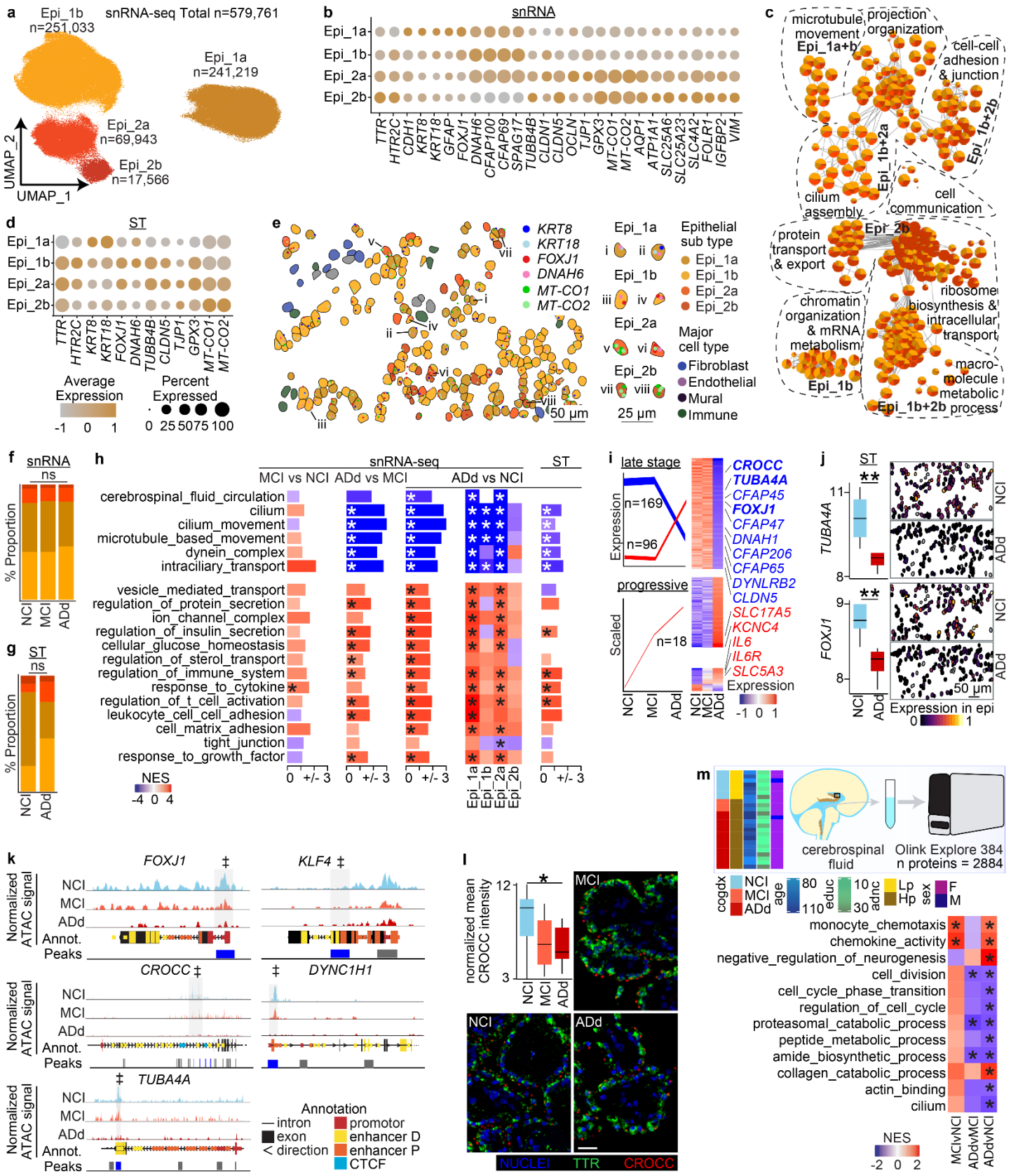
a
Epi_1b n=251,033
snRNA-seq Total n=579,761
Epi_1a n=241,219
Epi_2a n=69,943
Epi_2b n=17,566
UMAP_2
UMAP_1
b
snRNA
Epi_1a
Epi_1b
Epi_2a
Epi_2b
TTR HTR2C CDH1 KRT8 KRT18 GFAP FOXJ1 DNAH6 CFAP100 CFAP69 SPAG17 TUBB4B CLDN1 CLDN5 OCLN TJP1 GPX3 MT-CO1 MT-CO2 AQP1 ATP1A1 SLC25A6 SLC25A23 SLC4A2 FOLR1 IGFBP2 VIM
c
microtubule movement
projection organization
Epi_1a+b
cell-cell adhesion & junction
Epi_1b+2a
Epi_1b+2b
cilium assembly
cell communication
Epi_2b
protein transport & export
ribosome biosynthesis & intracellular transport
chromatin organization & mRNA metabolism
macro-molecule metabolic process
Epi_1b
Epi_1b+2b
d
ST
Epi_1a
Epi_1b
Epi_2a
Epi_2b
TTR HTR2C KRT8 KRT18 FOXJ1 DNAH6 TUBB4B CLDN5 TJP1 GPX3 MT-CO1 MT-CO2
Average Expression
-1 0 1
Percent Expressed
0 25 50 75 100
e
KRT8
KRT18
FOXJ1
DNAH6
MT-CO1
MT-CO2
50 µm
Epi_1a
Epi_1b
Epi_2a
Epi_2b
25 µm
Epithelial sub type
Epi_1a
Epi_1b
Epi_2a
Epi_2b
Major cell type
Fibroblast
Endothelial
Mural
Immune
f
snRNA
ns
% Proportion
NCI MCI ADd
g
ST
ns
% Proportion
NCI ADd
h
snRNA-seq
MCI vs NCI
ADd vs MCI
ADd vs NCI
ST
cerebrospinal_fluid_circulation
cilium
cilium_movement
microtubule_based_movement
dynein_complex
intraciliary_transport
vesicle_mediated_transport
regulation_of_protein_secretion
ion_channel_complex
regulation_of_insulin_secretion
cellular_glucose_homeostasis
regulation_of_sterol_transport
regulation_of_immune_system
response_to_cytokine
regulation_of_t_cell_activation
leukocyte_cell_cell_adhesion
cell_matrix_adhesion
tight_junction
response_to_growth_factor
NES
-4 0 4
0 +/- 3
Epi_1a Epi_1b Epi_2a Epi_2b
i
late stage
Expression
n=169
n=96
progressive
Scaled
n=18
NCI MCI ADd
CROCC
TUBA4A
CFAP45
FOXJ1
CFAP47
DNAH1
CFAP206
CFAP65
DYNLRB2
CLDN5
SLC17A5
KCNC4
IL6
IL6R
SLC5A3
Expression
-1 0 1
j
ST
TUBA4A
FOXJ1
NCI
ADd
50 µm
Expression in epi
0 1
k
FOXJ1
KLF4
CROCC
DYNC1H1
TUBA4A
Normalized ATAC signal
NCI
MCI
ADd
Annot.
Peaks
Annotation
intron
exon
direction
promotor
enhancer D
enhancer P
CTCF
l
normalized mean CROCC intensity
12
3
NCI MCI ADd
MCI
NCI
ADd
NUCLEI TTR CROCC
m
cerebrospinal fluid
Olink Explore 384
n proteins = 2884
cogdx NCI MCI ADd
age 80 110
educ 10 30
adnc Lp Hp
sex F M
monocyte_chemotaxis
chemokine_activity
negative_regulation_of_neurogenesis
cell_division
cell_cycle_phase_transition
regulation_of_cell_cycle
proteasomal_catabolic_process
peptide_metabolic_process
amide_biosynthetic_process
collagen_catabolic_process
actin_binding
cilium
MCIvNCI
ADdvMCI
ADdvNCI
NES
-2 0 2

Fig. 2: Progressive epithelial inflammation and late ciliary loss in Alzheimer's disease

a, snRNA-seq UMAP projection colored by epithelial subtypes.

b, Epithelial subtype-defining marker dot plot (FDR < 0.01, $\log_2$FC > 0.25). See Extended Data Table 7.

c, Epithelial subtype GO enrichment network plot (ClueGO on subtype-defining markers) grouped by functional category.

d, Unsupervised spatial transcriptomics (ST) confirmation of epithelial subtype-defining marker dot plot. See Extended Data Table 8.

e, Spatial localization of epithelial subtypes overlaid with subtype-defining transcript localization; FOV: 1.186. Scale bar: 50µm. Right: Selected examples. Scale bar: 25 µm.

f-g, snRNA-seq (f) and spatial transcriptomics (g) epithelial subtype proportions across disease states. Linear mixed model on proportions (* FDR < 0.01).

h, Select GO pathways (via fgsea on ranked t statistics) of DEGs throughout clinical disease in snRNA-seq (SN) and matched spatial transcriptomics (ST) (*FDR < 0.15). See Extended Data Table 10-12.

i, Disease temporal dynamics of DEGs. "Late-stage specific" genes: ADd ≠ NCI & MCI; "progressive" genes: NCI ≠ MCI & ADd and MCI ≠ ADd. Left: line plots indicate the mean of scaled gene expression; line width corresponds to the number of genes following each trajectory. Right: heatmap per stage select genes representing key GO pathways are labelled (nominal p < 0.05, $\log_2$FC > ±0.25, trajectory correlation p < 0.05).

j, Spatial transcriptomics expression of select cilia genes (left: quantification boxplot, median, interquartile range, min/max, ** FDR < 0.01; right: normalized expression in epithelial cells in example FOVs for NCI or ADd). Scale bars, 50 µm.

k, Differentially accessible chromatin peaks of select cilia genes throughout clinical disease progression (‡ nominal p<0.05 ADd vs NCI). Genome-specific annotations and accessible peaks are shown below. See Extended Data Table 13.

l, Mean CROCC intensity per TTR+ epithelial cell normalized to Hoechst intensity. Upper left: box plots throughout clinical disease progression (median, interquartile range, min/max; n = 9 NCI, 12 MCI, 9 ADd). One-way ANOVA $F_{(2,27)} = 4.135$, p<0.05; Tukey's HSD * p<0.05. Right/lower: representative immunohistochemistry of DAPI, TTR and CROCC per group. Scale bar: 50 µm.

m, Selected GO pathways of CSF protein data throughout clinical disease progression (via fgsea on ranked t statistics; * FDR < 0.15). See Extended Data Table 14.

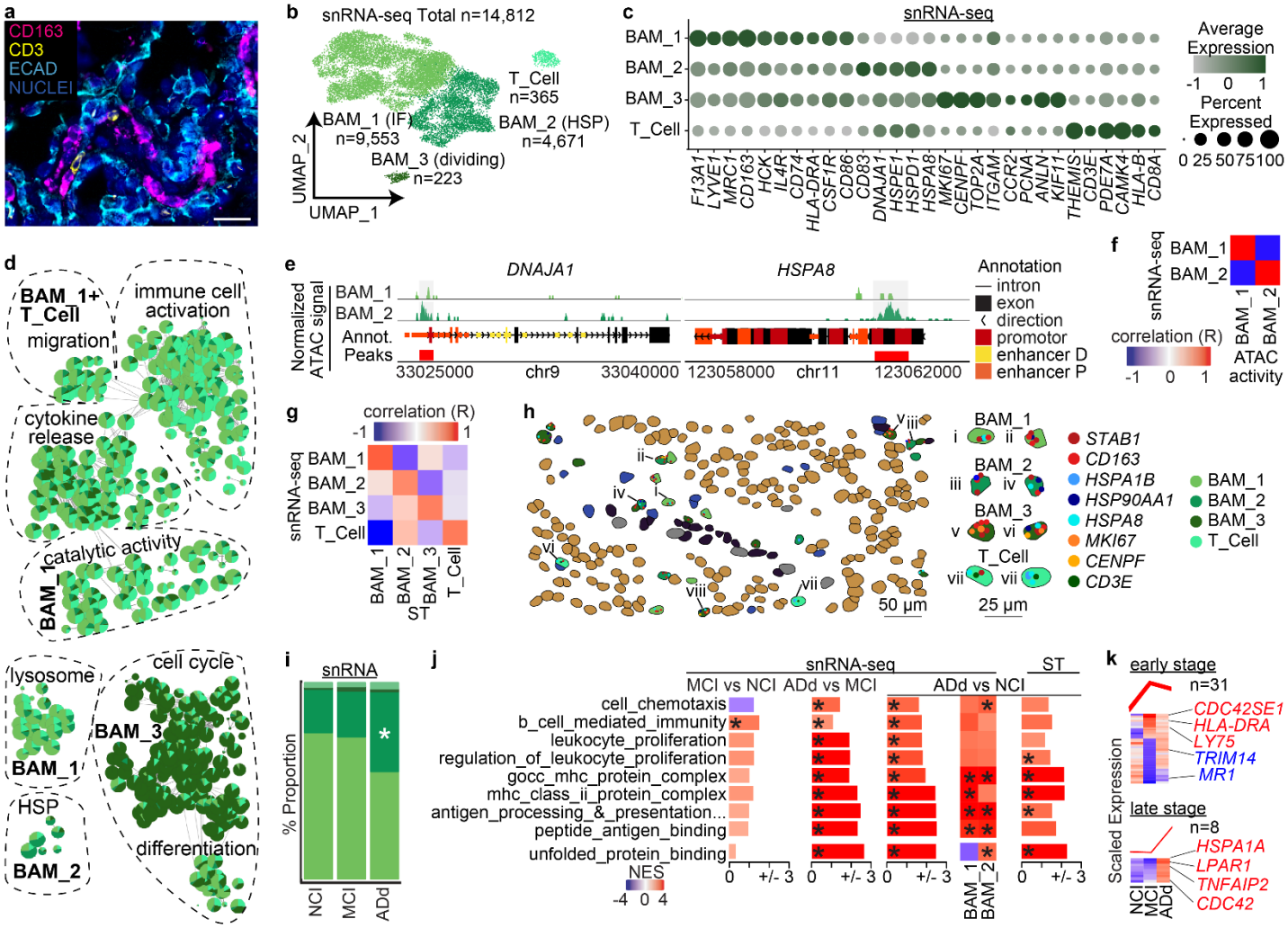
a
CD163
CD3
ECAD
NUCLEI
b
snRNA-seq Total n=14,812
T_Cell n=365
BAM_1 (IF) n=9,553
BAM_2 (HSP) n=4,671
BAM_3 (dividing) n=223
UMAP_2
UMAP_1
c
snRNA-seq
BAM_1
BAM_2
BAM_3
T_Cell
F13A1 LYVE1 MRC1 CD163 HCK IL4R CD74 HLA-DRA CSF1R CD86 CD83 DNAJA1 HSPE1 HSPD1 HSPA8 MKI67 CENPF TOP2A ITGAM CCR2 PCNA ANLN KIF11 THEMIS CD3E PDE7A CAMK4 HLA-B CD8A
Average Expression
-1 0 1
Percent Expressed
0 25 50 75 100
d
BAM_1+ T_Cell
immune cell activation
migration
cytokine release
catalytic activity
BAM_1
lysosome
cell cycle
BAM_3
BAM_1
HSP
BAM_2
differentiation
e
DNAJA1
HSPA8
Normalized ATAC signal
BAM_1
BAM_2
Annot.
Peaks
33025000 chr9 33040000
123058000 chr11 123062000
Annotation
intron
exon
direction
promotor
enhancer D
enhancer P
f
snRNA-seq
BAM_1
BAM_2
correlation (R)
-1 0 1
ATAC activity
g
correlation (R)
-1 1
snRNA-seq
BAM_1
BAM_2
BAM_3
T_Cell
ST
h
i ii iii iv v vi vii viii
50 µm
25 µm
STAB1
CD163
HSPA1B
HSP90AA1
HSPA8
MKI67
CENPF
CD3E
BAM_1
BAM_2
BAM_3
T_Cell
i
snRNA
% Proportion
NCI MCI ADd
j
snRNA-seq
ST
MCI vs NCI
ADd vs MCI
ADd vs NCI
cell_chemotaxis
b_cell_mediated_immunity
leukocyte_proliferation
regulation_of_leukocyte_proliferation
gocc_mhc_protein_complex
mhc_class_ii_protein_complex
antigen_processing_&_presentation...
peptide_antigen_binding
unfolded_protein_binding
NES
-4 0 4
0 +/- 3
BAM_1 BAM_2
k
early stage
n=31
CDC42SE1
HLA-DRA
LY75
TRIM14
MR1
late stage
n=8
HSPA1A
LPAR1
TNFAIP2
CDC42
Scaled Expression
NCI MCI ADd
l
ST
NCI
ADd
HSP90B1
HSPA1B
HSP90AA1
50 µm
HSP90B1
HSP90AA1
HSPA1B
NCI ADd
m
ST
NCI
ADd
CD68
HLA-DRA
HLA-DRB
50 µm
CD68
HLA-DRA
HLA-DRB
NCI ADd
n
NCI MCI ADd
CD163
CAV
HLA-DR
CD68
CD68 intensity in CD163+ cells
HLA-DR intensity in CD163+ cells
ns
NCI MCI ADd
o
ADd
CD3
CD3+ Tcells/mm²
NCI MCI ADd

921 **Fig. 3: Border-associated macrophages shifted from inflammatory to stress-associated states in Alzheimer's disease**
922 **a,** Phenocycler fusion multiplexed immunostaining of DAPI, CD163, CD3 and E-cadherin (ECAD). Scale bar: 50µm.
923 **b,** snRNA-seq UMAP of immune cell subclusters.
924 **c,** Immune subtype defining marker dot plot (FDR < 0.01, $\log_2$ fold change > 0.25). See Table Extended Data Table 15.
925 **d,** Immune subtype GO enrichment network plot (ClueGo on subtype-defining markers) grouped by functional category
926 and color-coded by immune subtype.
927 **e,** Differentially accessible chromatin peaks of select HSP genes per subtype. Genome-specific annotations and accessible
928 peaks are shown below.
929 **f,** Pearson correlation of chromatin accessibility (ATAC activity) and snRNA-seq expression among shared immune
930 substates.
931 **g,** Pearson correlation of supervised spatial transcriptomics (ST) and snRNA-seq expression among immune substates.
932 **h,** Spatial localization of immune subtypes overlaid with subtype-defining marker expression; FOV: 1.186. Scale bar:
933 50µm. Right: Selected examples. Scale bar: 25 µm.
934 **i,** Subtype proportions stratified by clinical diagnosis (* BAM_2 FDR < 0.01).
935 **j,** Select GO pathways (via fgsea on ranked t statistics) of DEGs throughout clinical disease in snRNA-seq and matched
936 spatial transcriptomics (*FDR < 0.15). See Extended Data Table 17-19.
937 **k,** Disease temporal dynamics of DEGs. "early stage" genes: NCI vs. MCI; "Late-stage specific" genes: ADd ≠ NCI &
938 MCI. Upper: line plots indicate the mean of scaled gene expression; line width corresponds to the number of genes
939 following each trajectory. Lower: heatmap per stage; select genes representing key GO pathways are labelled ($p < 0.05$,
940 $\log_2FC > \pm 0.25$, trajectory correlation $p < 0.05$).
941 **l-m,** Spatial transcriptomics gene expression of select HSP (**l**) and inflammation (**m**) Left: box plots (median, interquartile
942 range, min/max, ‡ nominal $p < 0.05$). Right: Spatial localization of expression in NCI FOV #1.168 and AD FOV #2.24.
943 Scale bar: 50 µm.
944 **n,** Left: Representative Phenocycler fusion immunofluorescence of HLA-DR and CD68, or CD163 and caveolin (CAV)
945 with DAPI for NCI and ADd. Scale bar: 50µm. Right: box plots of mean HLA-DR or CD68 intensity within CD163+
946 cells in NCI or ADd (median, interquartile range, and full range, *$p \leq 0.05$). Welch's test HLA-DR: p=0.0582; CD68:
947 p=0.01.
948 **o,** Representative Phenocycler fusion immunofluorescence of DAPI, CD3 and CD163. Scale bar, 50µm. Right: Box plot
949 of the numbers of CD4+ and CD8+ CD3+ T cells in NCI or ADd tissue (median, interquartile range, and full range). Non-
950 significant (ns).
951

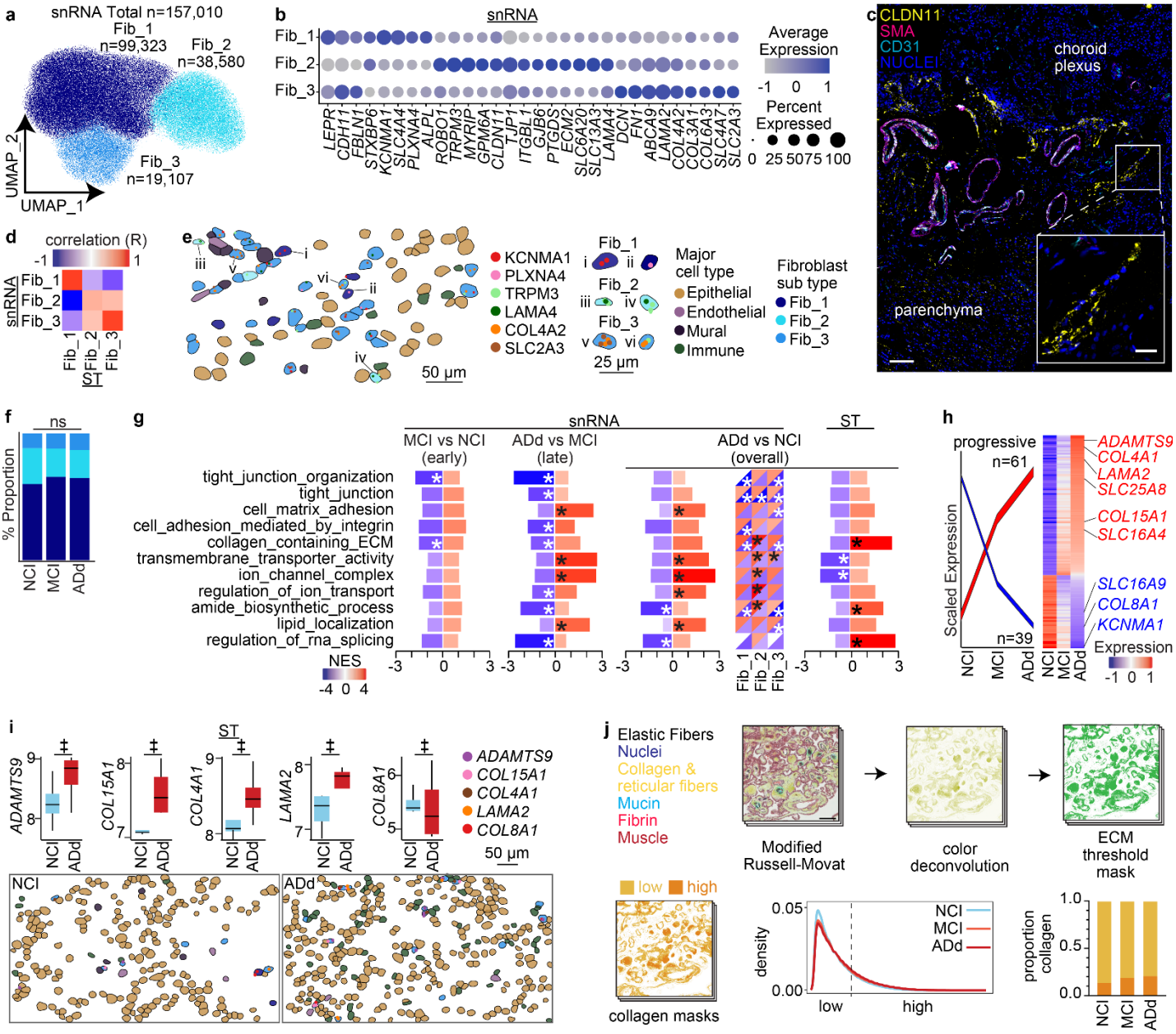
a
snRNA Total n=157,010
Fib_1
n=99,323
Fib_2
n=38,580
Fib_3
n=19,107
UMAP_2
UMAP_1
b
snRNA
Fib_1
Fib_2
Fib_3
LEPR CDH11 FBLN1 STXBP6 KCNMA1 SLC4A4 PLXNA4 ALPL ROBO1 TRPM3 MYRIP GPM6A CLDN11 TJP1 ITGBL1 GJB6 PTGDS ECM2 SLC6A20 SLC13A3 LAMA4 DCN FN1 ABCA9 LAMA2 COL4A2 COL3A1 COL6A3 SLC4A7 SLC2A3
Average Expression
-1 0 1
Percent Expressed
0 25 50 75 100
c
CLDN11
SMA
CD31
NUCLEI
choroid plexus
parenchyma
d
correlation (R)
-1 1
snRNA
Fib_1
Fib_2
Fib_3
ST
e
i
ii
iii
iv
v
vi
50 µm
KCNMA1
PLXNA4
TRPM3
LAMA4
COL4A2
SLC2A3
Fib_1
Fib_2
Fib_3
25 µm
Major cell type
Epithelial
Endothelial
Mural
Immune
Fibroblast sub type
Fib_1
Fib_2
Fib_3
f
ns
% Proportion
NCI
MCI
ADd
g
snRNA
ST
MCI vs NCI (early)
ADd vs MCI (late)
ADd vs NCI (overall)
tight_junction_organization
tight_junction
cell_matrix_adhesion
cell_adhesion_mediated_by_integrin
collagen_containing_ECM
transmembrane_transporter_activity
ion_channel_complex
regulation_of_ion_transport
amide_biosynthetic_process
lipid_localization
regulation_of_rna_splicing
NES
-4 0 4
-3 0 3
Fib_1
Fib_2
Fib_3
h
progressive
n=61
n=39
Scaled Expression
NCI
MCI
ADd
ADAMTS9
COL4A1
LAMA2
SLC25A8
COL15A1
SLC16A4
SLC16A9
COL8A1
KCNMA1
Expression
-1 0 1
i
ST
ADAMTS9
COL15A1
COL4A1
LAMA2
COL8A1
NCI
ADd
50 µm
j
Elastic Fibers
Nuclei
Collagen & reticular fibers
Mucin
Fibrin
Muscle
Modified Russell-Movat
color deconvolution
ECM threshold mask
low
high
collagen masks
density
0.05
0.00
NCI
MCI
ADd
low
high
proportion collagen
1.0
0.5
0.0

964 **Fig. 4: Fibroblast subtypes and remodeling in Alzheimer's Disease**
965 **a**, snRNA-seq UMAP projection colored by fibroblast subtypes.
966 **b**, Fibroblast subtype-defining marker dot plot (FDR < 0.01, $\log_2$FC > 0.25). See Extended Data Table 19.
967 **c**, Multiplexed Opal immunohistochemistry for DAPI, CLDN11, CD31 and SMA, showing localization of CLDN11-
968 positive cells at the boundary between CP and parenchyma. Scale bars = 100µm (overview), 20µm (inset).
969 **d,** Pearson correlation of supervised spatial transcriptomics (ST) and snRNA-seq expression among fibroblast subtypes.
970 **e**, Spatial localization of fibroblast subtypes overlaid with subtype-defining marker expression; FOV: 2.160. Scale bar:
971 50µm. Higher magnification on right. Right: Selected examples. Scale bar: 25 µm.
972 **f,** Subtype proportions stratified by clinical diagnosis Linear mixed model on proportions (all not significant, FDR > 0.01,
973 ns).
974 **g**, Select GO pathways (via fgsea on ranked t statistics) of DEGs throughout clinical disease in snRNA-seq and matched
975 spatial transcriptomics (* FDR < 0.15). See Extended Data Table 20-22.
976 **h**, Disease temporal dynamics of DEGs. "progressive" genes: NCI ≠ MCI & ADd and MCI ≠ ADd. Left: line plots
977 indicate the mean of scaled gene expression; line width corresponds to the number of genes following each trajectory.
978 Right: heatmap per stage select genes representing key GO pathways are labelled (nominal $p < 0.05$, $\log_2$FC > ±0.25,
979 trajectory correlation $p < 0.05$).
980 **i,** Spatial transcriptomic expression of select ECM genes. Upper: quantification boxplot (median, interquartile range,
981 min/max, ‡ nominal $p < 0.05$; bottom: transcript localization in fibroblasts in NCI FOV #1.86 and ADd FOV #2.119.
982 Scale bar: 50 µm).
983 **j**, Upper and lower left: Representative Modified Russel-Movat's stain, deconvoluted yellow (collagen), and ECM
984 threshold mask (< 230 pixel intensity), and high and low collagen masks (230-200, 200-0) (Scale bar: 100µm). Lower
985 middle: averaged distribution of collagen intensity colored by disease stage. Lower right: Stacked barchart of the
986 proportion of high and low collagen by disease stage. n = 8 NCI, 10 MCI, 9 ADd, 5-10 FOVs per subject.
987
988
989
990
991
992

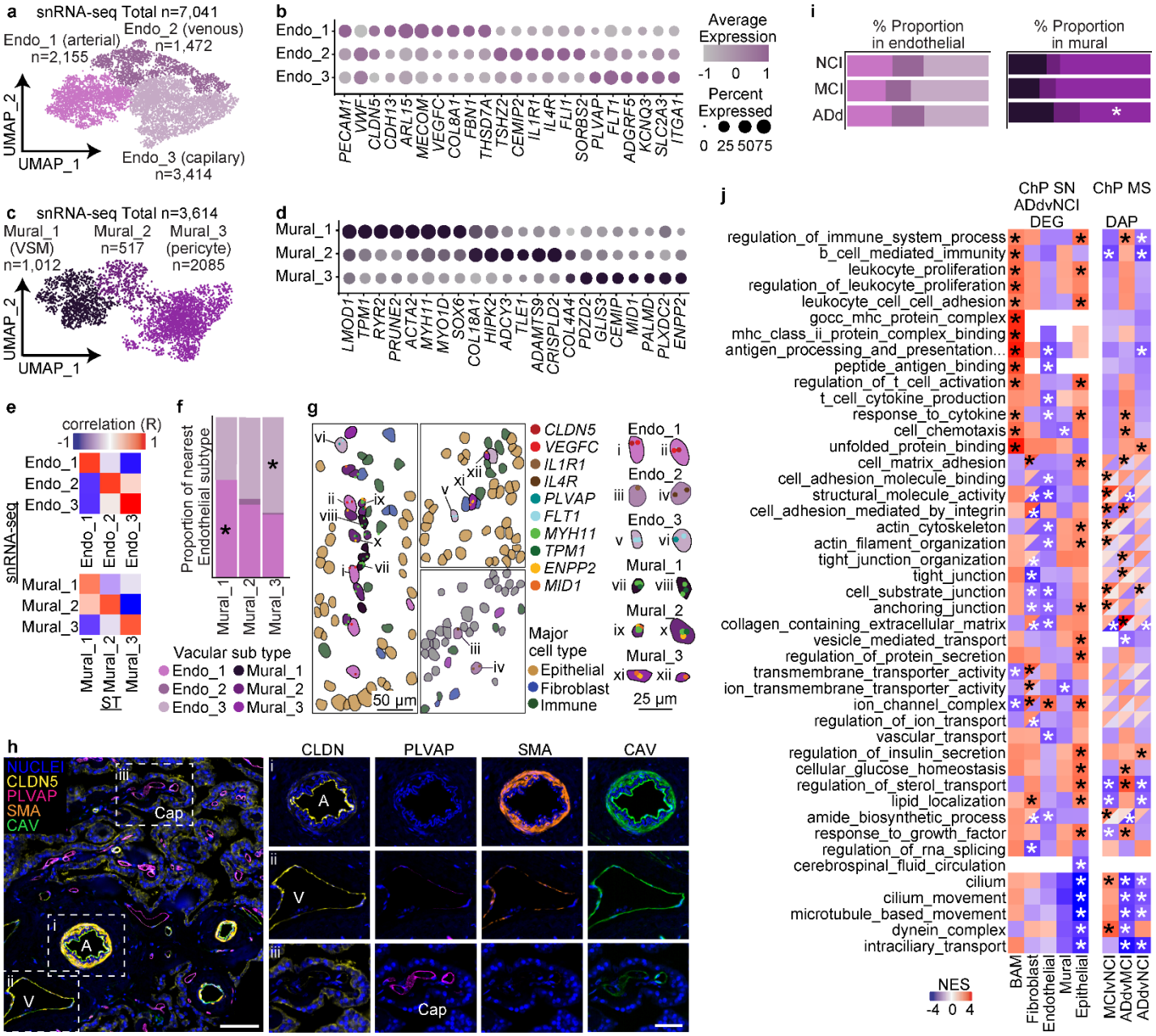

Fig. 5: Endothelial and mural cell dysregulation in Alzheimer's Disease

a, & c, snRNA-seq UMAP colored by endothelial (a) and mural (c) subtypes.

b, & d, Endothelial (b) and mural (d) subtype-defining marker dot plot (FDR < 0.01, $\log_2$FC > 0.25). See Extended Data Tables 22-23.

e, Pearson correlation of supervised spatial transcriptomics (ST) to snRNA-seq expression pooled among endothelial (upper) and mural (lower) subtypes.

f, Proportion of nearest endothelial subtype across Mural subtypes. Linear mixed model on proportions (* $p < 0.05$).

g, Spatial localization of endothelial and mural subtypes overlaid with subtype-defining marker expression; FOV: 1.186; Scale bar: 50µm. Right: Selected examples. Scale bar: 25 µm.

h, Phenocycler fusion immunofluorescence of endothelial (CLDN5, CAV, PLVAP) and mural (SMA) with DAPI. Capillary (Cap), arterial (A), and vascular venous(V) structures indicated and split by stain on right.

i, Endothelial (left) and mural (right) subtype proportions stratified by clinical diagnosis. Scale bars = 100µm (overview), 50µm (insets); Mural_3 * FDR < 0.01, others not significant.

j, Select GO pathways (via fgsea on ranked t statistics) of ADd vs NCI DEGs across all major cell types matched to mass spectrophotometry proteomics throughout clinical disease (*FDR < 0.15). See Extended Data Tables 24-28.

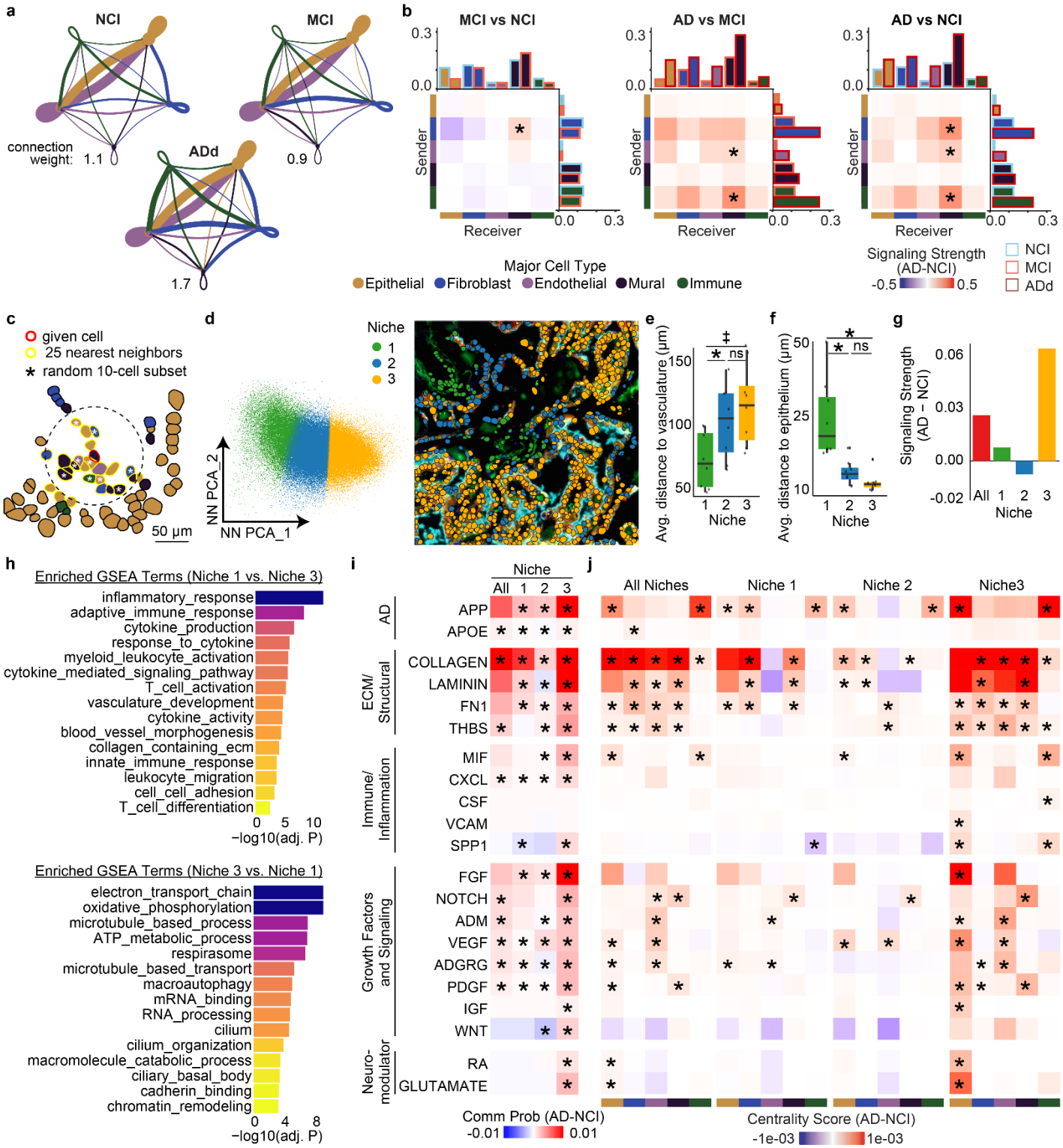
a
NCI
MCI
ADd
connection weight:
1.1
0.9
1.7
b
MCI vs NCI
AD vs MCI
AD vs NCI
Sender
Receiver
Major Cell Type
Epithelial
Fibroblast
Endothelial
Mural
Immune
Signaling Strength (AD-NCI)
-0.5
0.5
NCI
MCI
ADd
c
given cell
25 nearest neighbors
random 10-cell subset
50 µm
d
Niche
1
2
3
NN PCA_2
NN PCA_1
e
Avg. distance to vasculature (µm)
Niche
ns
f
Avg. distance to epithelium (µm)
Niche
ns
g
Signaling Strength (AD - NCI)
Niche
h
Enriched GSEA Terms (Niche 1 vs. Niche 3)
inflammatory_response
adaptive_immune_response
cytokine_production
response_to_cytokine
myeloid_leukocyte_activation
cytokine_mediated_signaling_pathway
T_cell_activation
vasculature_development
cytokine_activity
blood_vessel_morphogenesis
collagen_containing_ecm
innate_immune_response
leukocyte_migration
cell_cell_adhesion
T_cell_differentiation
−log10(adj. P)
Enriched GSEA Terms (Niche 3 vs. Niche 1)
electron_transport_chain
oxidative_phosphorylation
microtubule_based_process
ATP_metabolic_process
respirasome
microtubule_based_transport
macroautophagy
mRNA_binding
RNA_processing
cilium
cilium_organization
macromolecule_catabolic_process
ciliary_basal_body
cadherin_binding
chromatin_remodeling
−log10(adj. P)
i
Niche
All
1
2
3
AD
APP
APOE
ECM/ Structural
COLLAGEN
LAMININ
FN1
THBS
Immune/ Inflammation
MIF
CXCL
CSF
VCAM
SPP1
Growth Factors and Signaling
FGF
NOTCH
ADM
VEGF
ADGRG
PDGF
IGF
WNT
Neuro-modulator
RA
GLUTAMATE
Comm Prob (AD-NCI)
-0.01
0.01
j
All Niches
Niche 1
Niche 2
Niche3
Centrality Score (AD-NCI)
-1e-03
1e-03

Fig. 6: Altered CP intercellular communication in AD

a, AD differential CellChat inferred communication weights between major cell types throughout clinical disease progression in snRNA-seq.

b, AD differential CellChat net probability (CellChat net$prob) heatmaps among all ligand-receptor pairs in each colored sender-receiver pair (* $p < 0.05$).

c, Partial field of view (FOV #1.89), with cells colored by major cell type, to illustrate the nearest neighbor analysis approach. For each cell (e.g. red-outlined cell), a neighborhood transcriptome profile is calculated by averaging expression of a random 10-cell subset (white asterisks) of its 25 nearest neighbors (yellow-outline).

d, Left: UMAP representation of neighborhood expression matrix colored by cluster (k-means = 3). Right: spatial plot of FOV #1.89, with cells colored by niche identity overlaid on immunofluorescent image.

e-f, Boxplots of average cell to cell distances per niche to the nearest target cell type(s): Endothelial or Mural cell for (e), Epithelial cell for (f). Pairwise Wilcoxon tests with BH correction between niche (* $p < 0.05$, ‡ $p=0.07$, ns: not significant).

g, CellChat normalized AD-differential signaling strength bar charts.

h, Bar charts of select GO terms (via fgsea on ranked t statistic) for niche 1 (upper) and niche 3 (lower).

i, Interaction probability heatmap of select AD-differential CellChat pathways, for either the full or niche-specific datasets (* $p < 0.05$).

j, For the same pathways in (i), AD-differential signaling split by colored cell types, for either the full or niche-specific datasets (* $p < 0.05$)

1056 **Extended Data Figures**

1057

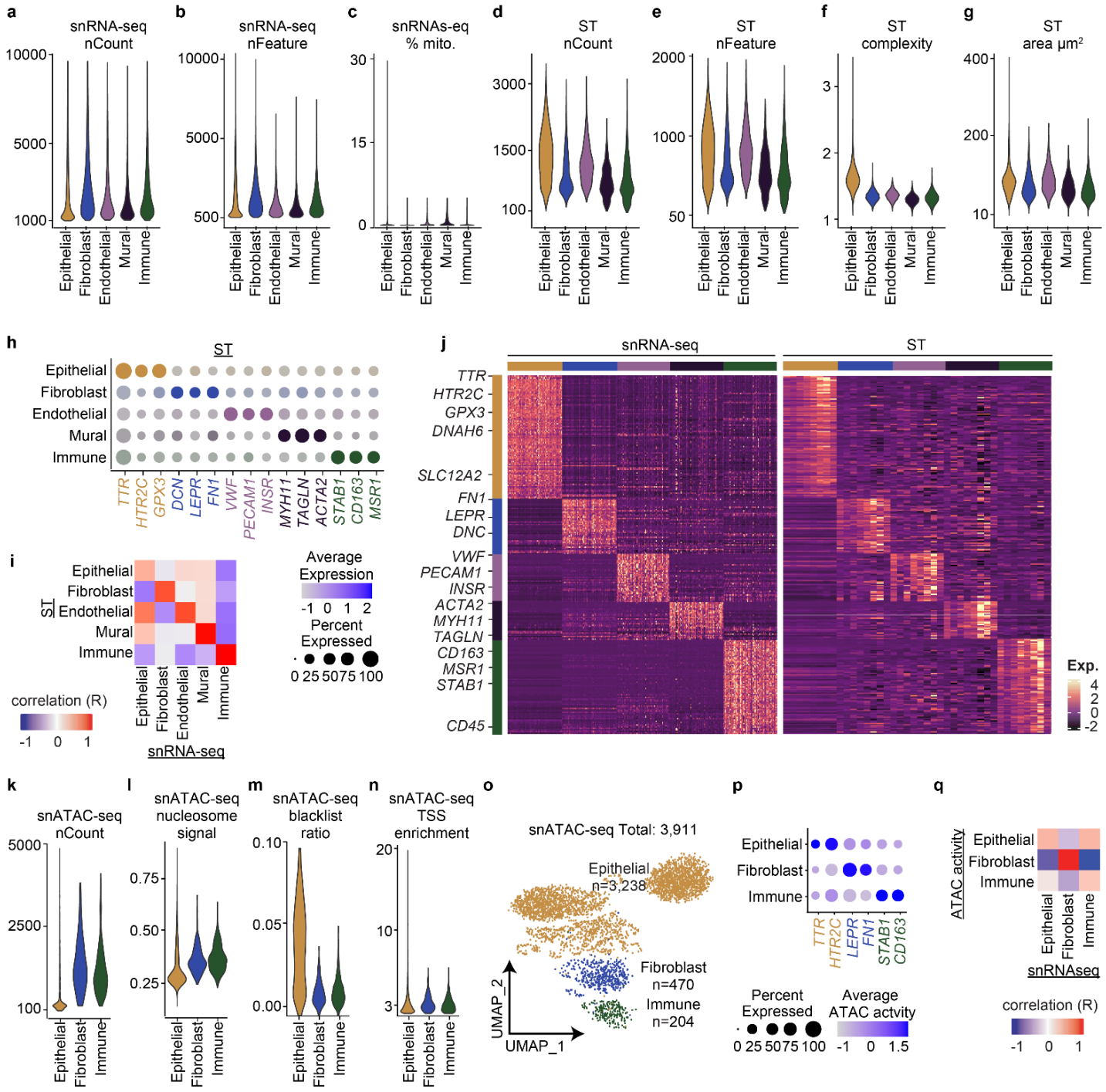

1058

1059

1060

1061

1062

1063

1064

1065

1066

1067

1068

Extended Data Fig. 1: QC and cell-type validation across snRNA-seq, ST ad snATAC-seq

a–c, Total RNA counts(a), number of detected features (b), and Mitochondrial read percentage (c) violin plots per snRNA-seq subtype.

d–g, Total RNA counts (a), number of detected features (b), segmented cell area (μm²; c) and complexity (d) violin plots per spatial transcriptomics (ST) subtype.

h, Unsupervised spatial transcriptomic confirmation of canonical marker expression dot plot across cell clusters. See Extended Data Table 4.

i, Pearson correlation of spatial trancriptomics to RNA expression pooled among major cell types.

j, Heatmap of marker gene expression identified in snRNA-seq (limma; FDR < 0.01, $\log_2$FC > 0.25) projected onto ST.

k-n, Total peaks counts (k), nucleosome_signal (l), blacklist_ratio (m), and TSS_enrichment (n) **violin plots per** snATAC-seq subtype.

o, UMAP projection of major celltypes with cell counts indicated.

p, Unsupervised snATAC-seq confirmation of canonical marker expression dot plot across cell clusters. See Extended Data Table 6.

q, Pearson correlation of chromatin accessibility to RNA expression pooled among major cell types.

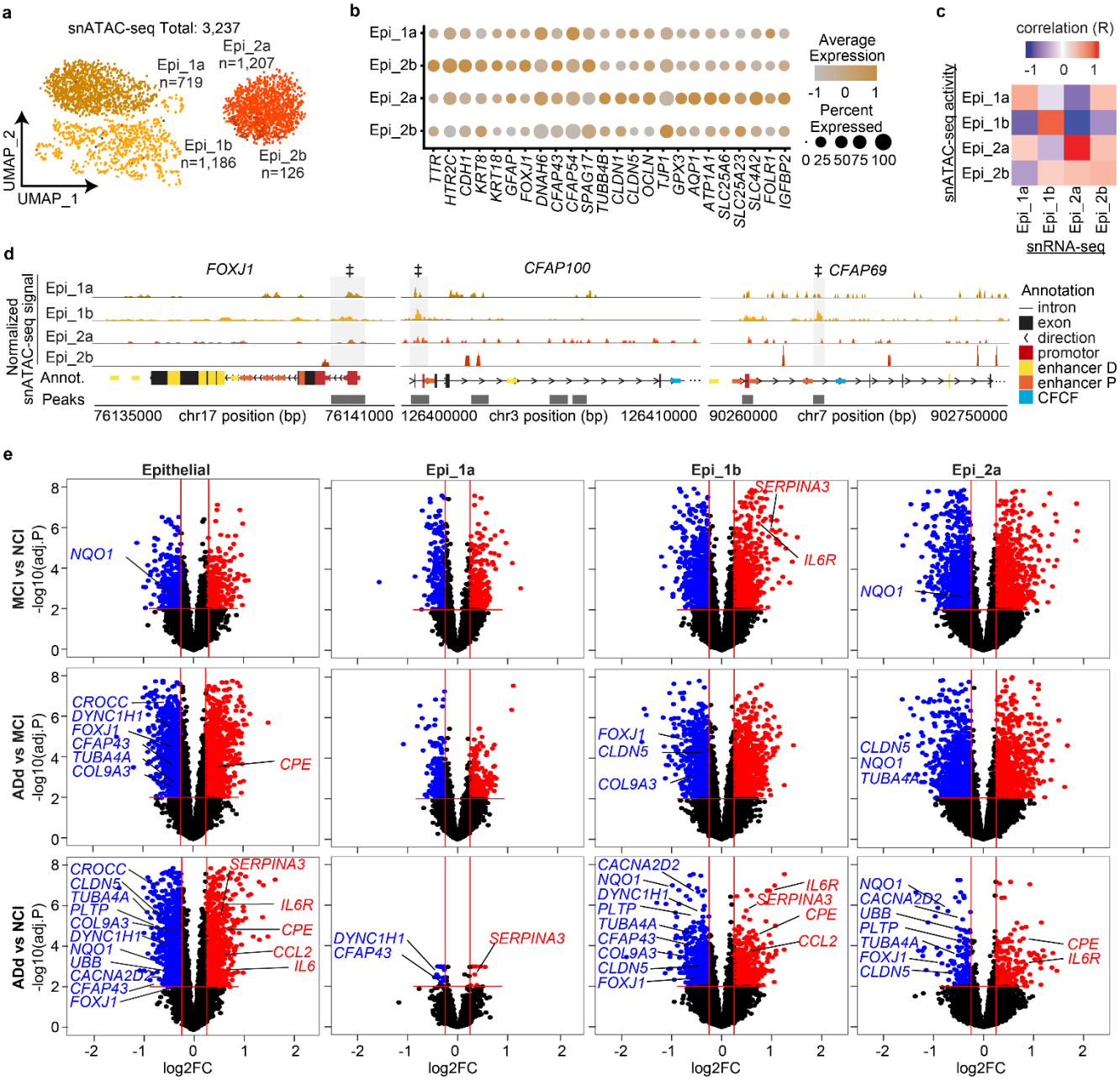

Extended Data Fig. 2: Epithelial cell subtypes defined by snATAC-seq and differential gene expression across disease stages

a, snATAC-seq UMAP colored by epithelial subtype.

b, Unsupervised snATAC-seq epithelial subtype-defining marker dot plot (FDR < 0.01, $\log_2$FC > 0.25). See Extended Data Table 9.

c, Pearson correlation of chromatin accessibility (ATAC activity) to RNA expression pooled among epithelial subtypes.

d, Differentially accessible chromatin peaks for select cilia genes per epithelial subtypes (‡ p<0.05). Genome specific annotations and accessible peaks are shown below.

e, snRNA-seq **e**pithelial and **s**ub type * disease specific DEG volcano plots. Select genes representing key GO pathways are labelled (all FDR < 0.01 and $\log_2$ fold change > ±0.25).

f, Scatter plots contrasting t-statistics from differential gene expression analysis between clinical stages (MCI vs NCI and ADd vs NCI), Select genes representing key GO pathways are labelled (all FDR < 0.01 and $\log_2$ fold change > ±0.25).

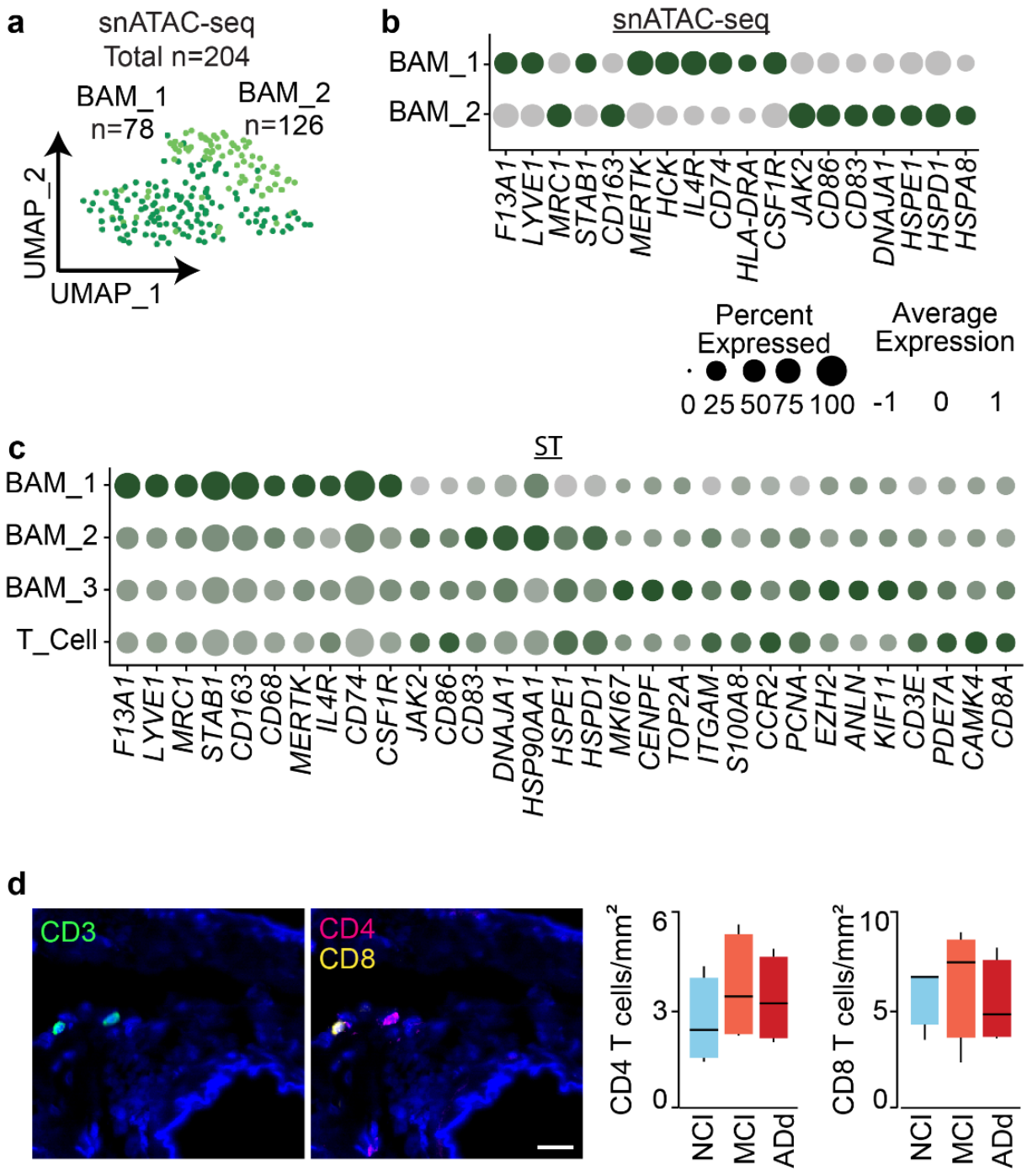

Extended Data Fig. 3: Immune cell subtypes defined by snATAC-seq and ST

a, snATAC-seq UMAP colored by immune subtypes.

b, Unsupervised snATAC-seq immune subtype-defining marker dot plot. See Extended Data Table 16.

c, Supervised spatial transcriptomics (ST) immune subtype-defining marker dot plot.

d, CD4 and CD8 staining and quantifications across NCI, MCI and AD groups.

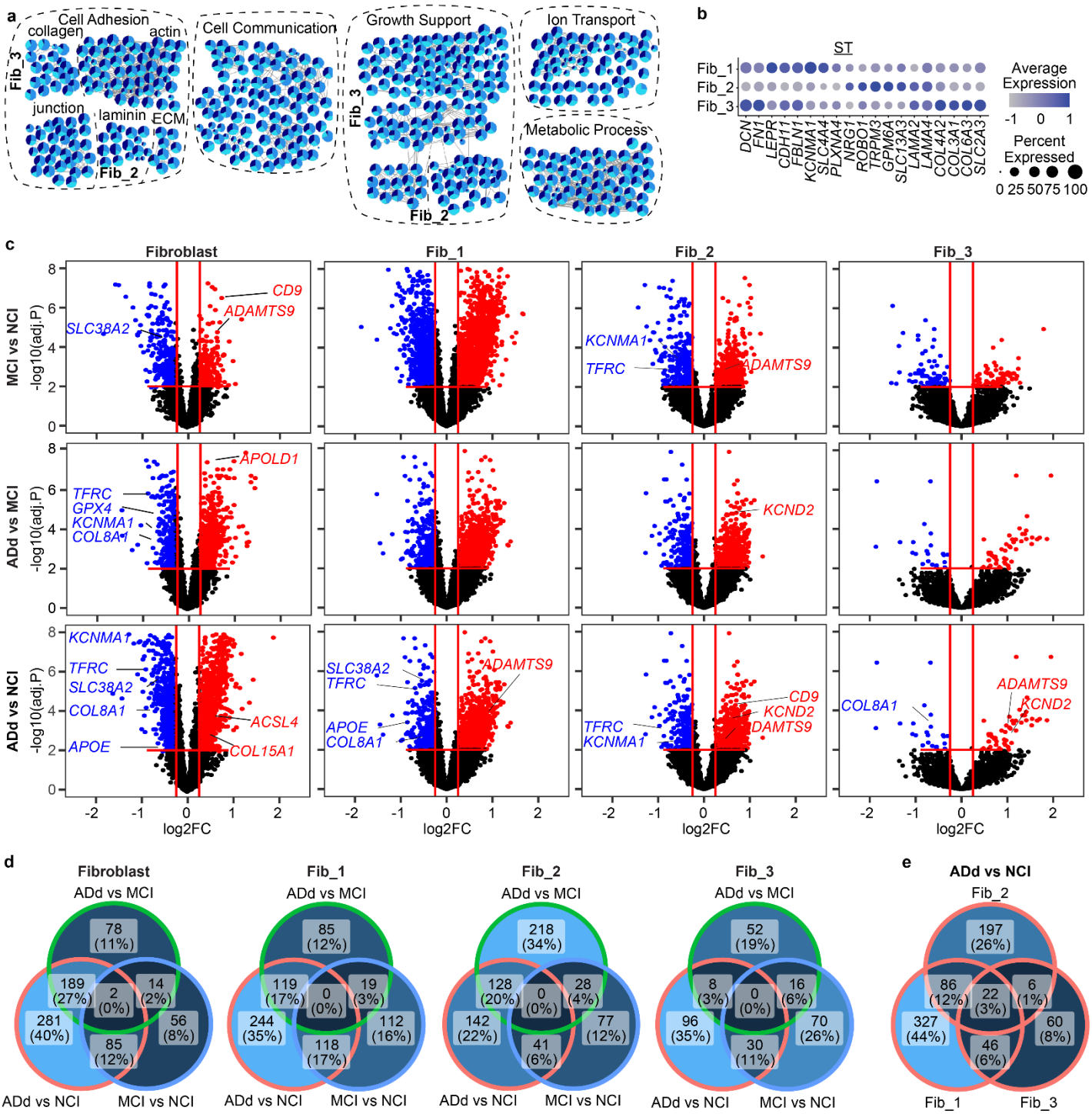

Extended Data Fig. 4: Fibroblast subtype-resolved differential gene expression across disease stages

a, Fibroblast subtype GO enrichment network plot (ClueGO on subtype-defining markers) grouped by functional category.

b, Supervised spatial transcriptomics (ST) fibroblast subtype-defining marker dot plot.

c, snRNA-seq fibroblast and sub type * disease specific DEG volcano plots. Select genes representing key GO pathways are labelled (all FDR < 0.01 and $\log_2$ fold change > ±0.25).

b, Overlap of differentially expressed genes across subtypes and disease stages.

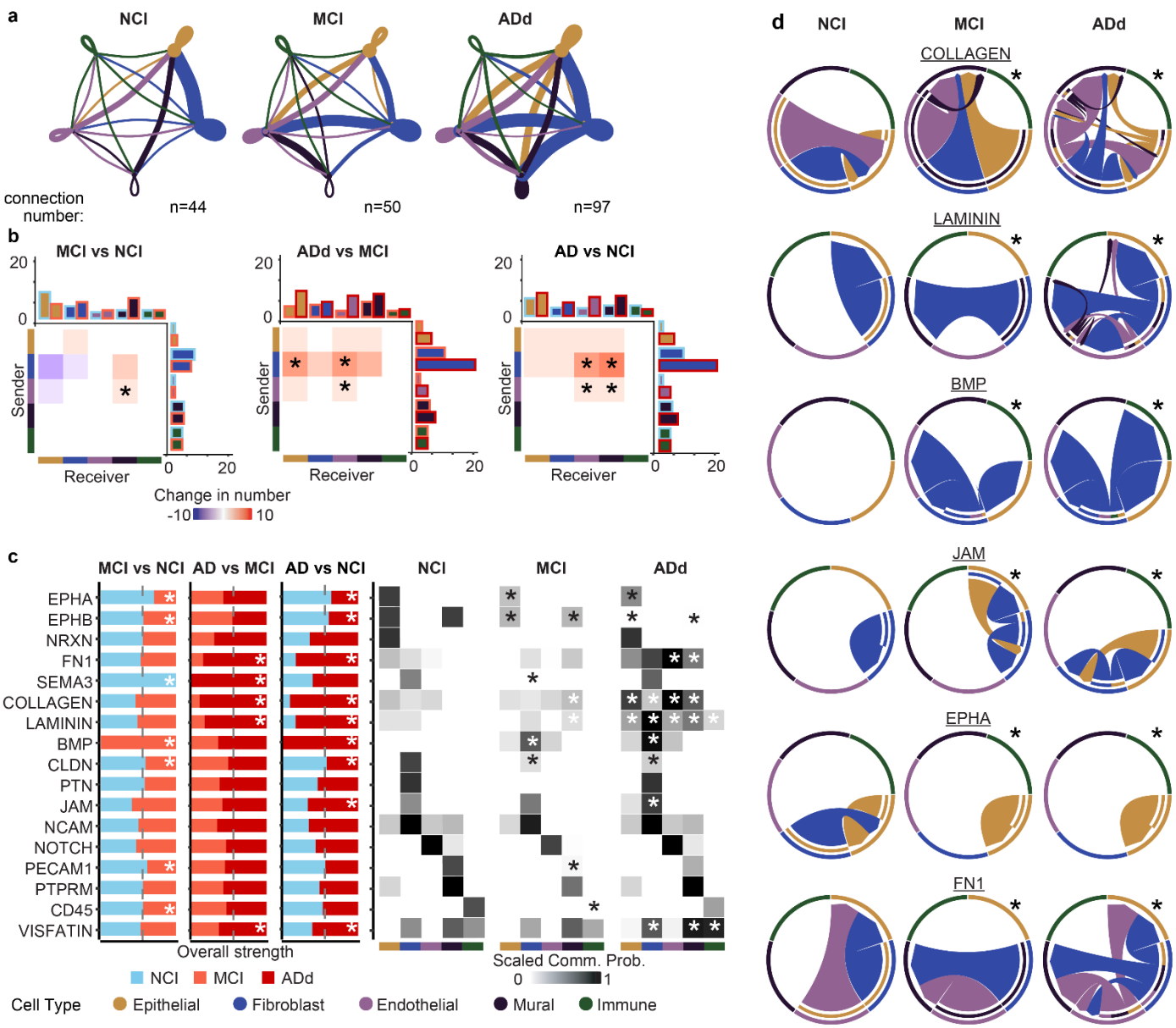

Extended Data Fig. 5: CellChat analysis of snRNA-seq data reveals altered CP intercellular communication in AD

a, Differential CellChat inferred communication number between major cell types throughout clinical disease progression in snRNA-seq.

b, AD differential CellChat communication number heatmaps among all ligand-receptor pairs in each colored sender-receiver pair (* $p < 0.05$).

c, Select signaling pathways mediating differential intercellular communication throughout clinical disease progression. Left: Total signaling strength histogram. Right: Scaled communication probability per cell type (* $p < 0.05$). See Extended Data Table 29.

d, Selected chord diagrams of intercellular signaling between major cell types throughout clinical disease progression (* $p < 0.05$).

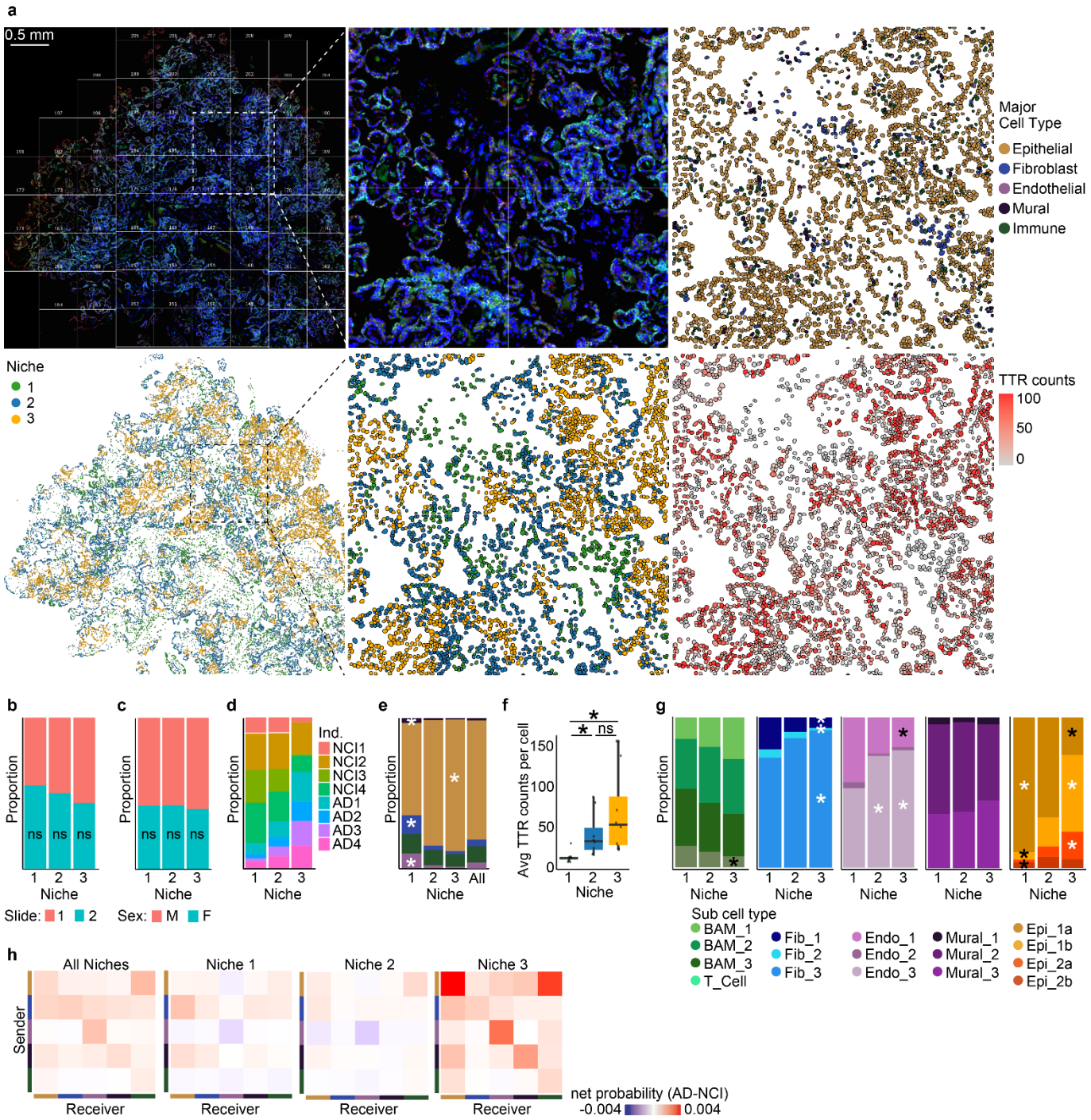

Extended Data Fig. 6: Niche-specific communication changes in Alzheimer's disease

a, Example tissue section immunofluorescent stain (upper left) colored by niche (lower left). Middle: Higher magnification of 4 FOVs. Upper right: Major cell type annotation. Lower left: TTR counts per cell type.

b-e, Stacked bar charts showing proportion of slide (b), sex (c), individual (d), major cell type (e) per niche. Linear mixed model on proportions (Mural, Fibroblast and Endothelial in niche 1, Epithelial in niche 3 * FDR < 0.05, ns: not significant).

f, Boxplot shows individual- and niche-specific pseudobulk expression of TTR (* p <0.001, ns: not significant).

g, Stacked bar charts showing subtype proportions per niche (* FDR < 0.05).

h, AD differential CellChat net probability (CellChat net$prob) heatmaps among all ligand-receptor pairs in each colored sender-receiver pair, for all cells (left), or subset by niche.

Extended Data Tables

Extended Data Table 1. Patient metadata

Extended Data Table 2. SN major celltype limma and GO

Extended Data Table 3. SN major and sub proportions and limma

Extended Data Table 4. ST major celltype limma and GO

Extended Data Table 5. ST major and sub proportions and limma

Extended Data Table 6. ATAC major celltype limma and GO

Extended Data Table 7. Epi SN subcelltype limma and GO

Extended Data Table 8. Epi ST subcelltype limma and GO

Extended Data Table 9. Epi ATAC subcelltype limma and GO

Extended Data Table 10. Epi SN major and sub cogdx and pattern limma and GO

Extended Data Table 11. Epi SN major and sub cog_dec limma and GO

Extended Data Table 12. Epi ST major cogdx limma and GO

Extended Data Table 13. Epi ATAC TF motifs subtype limma

Extended Data Table 14. CSF proteomic DEG limma and GO

Extended Data Table 15. Imm SN Excel subcelltype limma and GO

Extended Data Table 16. Imm ATAC subcelltype limma and GO

Extended Data Table 17. Imm SN major and sub cogdx and pattern limma and GO

Extended Data Table 18. Imm ST major and sub cogdx

Extended Data Table 19. Fib SN subcelltype limma and GO

Extended Data Table 20. Fib SN major and sub cogdx and pattern limma and GO

Extended Data Table 21. Fib ST major cogdx limma and GO

Extended Data Table 22. Endo SN Excel subcelltype limma and GO

Extended Data Table 23. Mural SN Excel subcelltype limma and GO

Extended Data Table 24. Endo SN major cogdx limma and GO

Extended Data Table 25. Endo ST major cogdx limma and GO

Extended Data Table 26. Mural SN major cogdx limma and GO

Extended Data Table 27. Mural ST major cogdx limma and GO

Extended Data Table 28. Proteomic Excel DEG limma and GO

Extended Data Table 29. SN and ST CellChat net_pathways and limma results

Extended Data Table 30. Cannonical markers and references